



1 **Quantification of the dust optical depth across spatiotemporal scales with the**
2 **MIDAS global dataset (2003-2017)**

3

4 Antonis Gkikas¹, Emmanouil Proestakis¹, Vassilis Amiridis¹, Stelios Kazadzis^{2,3}, Enza Di Tomaso⁴,
5 Eleni Marinou^{1,5}, Nikos Hatzianastassiou⁶, Jasper F. Kok⁷ and Carlos Pérez García-Pando^{4,8}

6

7 ¹Institute for Astronomy, Astrophysics, Space Applications and Remote Sensing, National Observatory of Athens,
8 Athens, 15236, Greece

9 ²Physikalisch-Meteorologisches Observatorium Davos, World Radiation Center, Switzerland

10 ³Institute of Environmental Research and Sustainable Development, National Observatory of Athens, Greece

11 ⁴Barcelona Supercomputing Center, Barcelona, Spain

12 ⁵Deutsches Zentrum für Luft- und Raumfahrt (DLR), Institut für Physik der Atmosphäre, Oberpfaffenhofen, Germany

13 ⁶Laboratory of Meteorology, Department of Physics, University of Ioannina, Ioannina, Greece

14 ⁷Department of Atmospheric and Oceanic Sciences, University of California, Los Angeles, CA 90095, USA

15 ⁸ICREA, Catalan Institution for Research and Advanced Studies, Barcelona, Spain

16

17
18 Corresponding author: Antonis Gkikas (agkikas@noa.gr)

19

20 **Abstract**

21 Quantifying the dust optical depth (DOD) and its uncertainty across spatiotemporal scales is key to
22 understanding and constraining the dust cycle and its interactions with the Earth System. This study
23 quantifies the DOD along with its monthly and year-to-year variability between 2003 and 2017 at
24 global and regional levels based on the MIDAS (ModIs Dust AeroSol) dataset, which combines
25 MODIS-Aqua retrievals and MERRA-2 reanalysis products. We also describe the annual and
26 seasonal geographical distributions of DOD across the main dust source regions and transport
27 pathways. MIDAS provides columnar mid-visible (550 nm) DOD at fine spatial resolution (0.1° x
28 0.1°), expanding the current observational capabilities for monitoring the highly variable
29 spatiotemporal features of the dust burden. We obtain a global DOD of 0.032 ± 0.003 – approximately
30 a quarter ($23.4\% \pm 2.4\%$) of the global AOD – with about one order of magnitude more DOD in the
31 northern hemisphere (0.056 ± 0.004 ; $31.8\% \pm 2.7\%$) than in the southern hemisphere (0.008 ± 0.001 ;
32 $8.2\% \pm 1.1\%$) and about 3.5 times more DOD over land (0.070 ± 0.005) than over ocean ($0.019 \pm$
33 0.002). The northern hemisphere monthly DOD is highly correlated with the corresponding monthly
34 AOD ($R^2=0.94$) and contributes 20% to 48% of it, both indicating a dominant dust contribution. In
35 contrast, the contribution of dust to the monthly AOD does not exceed 17% in the southern
36 hemisphere, although the uncertainty in this region is larger. Among the major dust sources of the
37 planet, the maximum DODs (~ 1.2) are recorded in the Bodélé Depression of the northern Lake Chad



38 Basin, whereas moderate-to-high intensities are encountered in the Western Sahara (boreal summer),
39 along the eastern parts of the Middle East (boreal summer) and in the Taklamakan Desert (spring).
40 Over oceans, major long-range dust transport is observed primarily along the Tropical Atlantic
41 (intensified during boreal summer) and secondarily in the North Pacific (intensified during boreal
42 spring). Our calculated global and regional averages and associated uncertainties are consistent with
43 some but not all recent observationally based studies. Our work provides a simple, yet flexible method
44 to estimate consistent uncertainties across spatiotemporal scales, which will enhance the use of the
45 MIDAS dataset in future studies.

46

47 1. Introduction

48 Mineral dust particles are emitted throughout the year across the arid and semi-arid regions of the
49 planet, when winds exceed a threshold velocity mainly determined by soil texture, soil moisture, and
50 surface roughness. While dust aerosols have mainly a natural origin, the contribution of
51 anthropogenic land use is estimated to be between 10% and 25 % (Tegen et al. 2004; Stanelle et al.,
52 2014; Ginoux et al., 2012). Dust is mobilized by microscale to synoptic scale phenomena, from dust
53 devils developed under strong surface heating (Koch and Renno, 2005), to “haboobs” formed by
54 intense cold-pool downdrafts related to deep moist convection (Knippertz et al., 2007), to synoptic
55 patterns associated with intensified pressure gradients (Klose et al., 2010) and low-level jets (LLJ;
56 Fiedler et al., 2013). Meteorology also plays a key role in the dust transport over maritime areas taking
57 place mainly across the Tropical Atlantic Ocean (Prospero and Mayol-Bracero, 2013; Yu et al., 2015),
58 the northern Pacific Ocean (Husar et al., 2001), the Mediterranean (Flaounas et al., 2015; Gkikas et
59 al., 2015), the Arabian Sea (Ramaswamy et al., 2017) and the southern Atlantic Ocean (Gasso and
60 Stein, 2007). Dust perturbs the radiation budget through direct (Sokolik and Toon, 1996), semi-direct
61 (Huang et al., 2006) and indirect (Haywood and Bucher, 2000) processes, leading to impacts upon
62 weather (Pérez et al., 2006; Gkikas et al., 2018; Gkikas et al., 2019) and climate (Lambert et al., 2013;
63 Nabat et al., 2015). Upon deposition, nutrient-rich dust particles can increase the productivity of
64 oceanic waters (Jickells et al., 2005) and terrestrial ecosystems (Okin et al., 2004) and perturb the
65 carbon cycle (Jickells et al., 2014). Dust has been associated with epidemics of meningococcal
66 meningitis in the African Sahel (Pérez García-Pando et al., 2014a, b) and with air quality degradation
67 in urban areas (Kanakidou et al., 2011) causing respiratory (Kanatani et al., 2010) and cardiovascular
68 (Du et al., 2016) disease when the population is exposed to high dust concentrations (Querol et al.,
69 2019). Other socio-economic sectors can be regionally affected by dust storms (Middleton, 2017),
70 including transportation (Weinzierl et al., 2012), agriculture (Stefanski and Sivakumar, 2009) and
71 solar energy production (Kosmopoulos et al., 2018).



72 Satellite measurements and numerical simulations have repeatedly shown the remarkable contrast
73 in dust load between the two hemispheres. The substantially higher dust load in the N. Hemisphere
74 is associated to the wider deserts extending across the so-called “dust belt” (Prospero et al., 2002;
75 Ginoux et al., 2012) in contrast to the smaller sources in Australia, South Africa and South America.
76 At global scale, most of the entrained dust loads in the atmosphere originate from tropical and sub-
77 tropical arid regions; yet, it is estimated that up to 5% of the global dust budget consists of particles
78 emitted from high-latitude sources (Bullard and Austin, 2011; Bullard et al., 2016). Given the key
79 role of dust aerosols in the Earth system it is imperative to monitor and understand the global dust
80 cycle along with its multi-scale spatiotemporal variability over long time periods and fine spatial
81 resolution. This task can be fulfilled to a certain degree using contemporary satellite instruments
82 providing accurate retrievals and global coverage over extended time periods. With this approach,
83 one of the key challenges is to discriminate dust from other aerosols. Several studies have combined
84 AOD and aerosol index (AI) (e.g., Middleton and Goudie, 2001; Prospero et al., 2002) or AOD, single
85 scattering albedo (SSA) and Angstrom exponent (AE) (Ginoux et al., 2012) to identify the most active
86 dust sources worldwide. Other studies have focused on the dust load and its variability in specific
87 regions such as the Atlantic Ocean and the Arabian Sea (Peyridieu et al., 2013), the Sistan basin
88 (Rashki et al., 2015), the Mediterranean (Gkikas et al., 2016), Europe and North Africa (Marinou et
89 al., 2017) and east Asia (Proestakis et al., 2018), among others. Liu et al. (2008) described the three-
90 dimensional structure of dust aerosols at global scale based on CALIOP vertically resolved retrievals
91 acquired during the first operational year of the CALIPSO satellite mission. A more advanced
92 approach has been introduced by Amiridis et al. (2013) and Marinou et al. (2017), who applied a
93 more realistic lidar ratio for the Saharan dust and a series of quality filters on the CALIOP vertical
94 profiles, in order to provide information about the vertical structure of dust layers at global scale and
95 coarse resolution in the LIVAS dataset (Amiridis et al., 2015). Ridley et al. (2016) quantified the
96 global average DOD and its uncertainty for the period 2004-2008 based on AOD retrievals from
97 passive spaceborne sensors (MODIS, MISR), ground-based (AERONET) and shipborne (MAN)
98 measurements from sun-photometers, and numerical simulations. Voss and Evan (2020) provided a
99 long-term DOD climatology over the Tropics and mid-latitudes at a coarse spatial resolution ($1^\circ \times$
100 1°) based on MODIS and AVHRR observations, where DOD was estimated based on: AOD, SSA
101 and AE over land following Ginoux et al. (2012) and AOD, fine and coarse AOD (AERONET) and
102 MERRA-2 winds over ocean. Based on vertically-resolved CALIOP retrievals and columnar MODIS
103 optical properties, Song et al. (2021) provided a long-term 4D global dust optical depth dataset,
104 excluding the polar regions, over the period 2007 – 2019. In their approach, they took advantage of
105 spaceborne observations that can be used for the discrimination/identification of dust aerosols
106 characterized by their aspherical shape, coarse size and absorption.



107 Our study provides a global and regional quantification and description of the DOD based on the
108 new ModIs Dust AeroSol (MIDAS) dataset (Gkikas et al., 2021). The powerful and innovative
109 elements of the MIDAS DOD dataset are the: (i) daily availability and fine spatial resolution ($0.1^\circ \times$
110 0.1°), (ii) full global coverage including the sources and downwind areas (both over land and sea),
111 (iii) 15-year temporal range (2003 – 2017) using the most updated MODIS data collection, (iv) grid-
112 cell level uncertainty quantification. In this contribution, we first describe the annual and seasonal
113 geographical distribution of DOD across the main dust source regions and transport pathways
114 (Section 4.1). We then quantify the average DOD and its monthly and year-to-year variability at
115 global, hemispherical and regional levels, along with its fractional contribution to the AOD (Section
116 4.2). We summarize the main findings in Section 5.

117 2. ModIs Dust AeroSol (MIDAS) dataset

118 Our study is based on the MIDAS global fine resolution dataset described in detail in Gkikas et
119 al. (2021). We analyse the DOD at 550 nm at $0.1^\circ \times 0.1^\circ$ spatial resolution between 2003 to 2017.
120 The MIDAS DOD results from the combination of the quality-filtered MODIS aerosol optical depth
121 (AOD, Collection 6.1, Level 2; Levy et al., 2013) and the MERRA-2 (Modern-Era Retrospective
122 Analysis for Research and Applications, version 2; Gelaro et al., 2017) fraction of AOD that is due
123 to dust (MDF). In Gkikas et al. (2021), the MDF was evaluated against the dust fraction obtained
124 from quality-assured dust and non-dust CALIOP (Cloud-Aerosol Lidar with Orthogonal Polarization;
125 Winker et al., 2009) profiles, available from the LIVAS database (Amiridis et al., 2015; Marinou et
126 al., 2017; Proestakis et al., 2018). The MDF compares well with the LIVAS dust fraction over the
127 dust-abundant areas extending across the NH dust belt, with maximum underestimations of 10 % in
128 Asian deserts. The agreement is more limited in North America and the Southern Hemisphere
129 (Figures 1 and 2 in Gkikas et al., 2021). Overall, the MIDAS DOD is well correlated with AERONET
130 dust-dominant retrievals ($R=0.89$ at global scale) and the absolute biases are mainly below 0.12 at
131 stations near sources (Figures 3 and 4 in Gkikas et al., 2021). The MIDAS DOD dataset was further
132 verified against the LIVAS DOD and compared with MERRA-2 DODs (Figure 5 in Gkikas et al.,
133 2021). Among the three datasets, there is good agreement on the monthly variability of the global and
134 hemispherical DODs as well as on their long-term averages (Figure 6 and Table 1 in Gkikas et al.,
135 2021). Moreover, the annual and seasonal DOD patterns are broadly similar in the three datasets
136 throughout the period 2007 – 2015. Nevertheless, regionally differences are found due to the different
137 techniques (passive and active remote sensing, numerical simulations) applied for the DOD
138 derivation.

139
140



141 3. Spatiotemporal averaging and propagation of grid-cell level uncertainties

142 In section 4.2 we provide DOD estimates that are averaged in space (regionally and globally) and
143 in time (over months, seasons and years) along with their respective uncertainties. Averaging is
144 performed according to the upper branch of Figure 5 in Levy et al. (2009), i.e. spatial averaging is
145 performed after grid cell temporal averaging for any of the timescales considered. The uncertainties
146 of the DOD averages at the different spatiotemporal scales are based on the propagation of the daily
147 grid cell uncertainties provided within the MIDAS dataset and presented in Gkikas et al. (2021). In
148 short, the daily grid cell uncertainties combine the uncertainties of the MODIS AOD and the
149 MERRA-2 MDF with respect to AERONET and LIVAS, respectively. The former is based on linear
150 equations expressing the uncertainty with respect to AERONET AOD over the ocean (Levy et al.,
151 2013) and land (Levy et al., 2010; Sayer et al. 2013) with updated coefficients for C061 data
152 depending on vegetated and arid surface types (see equations 4 to 7 in Gkikas et al., 2021). The latter
153 is based on a quartic (fourth degree) polynomial equation expressing the uncertainty with respect to
154 the LIVAS dust fraction (see equation 8 in Gkikas et al., 2021).

155 In order to estimate the uncertainties of the spatiotemporal averages we first assume that each of
156 the daily grid cell uncertainties are composed of (1) a fraction that is completely random in time and
157 space, (2) a fraction that is systematic (correlated) in time and random in space and (3) a fraction that
158 is systematic (correlated) in space and random in time. Our framework also assumes that the fraction
159 of the daily grid cell uncertainty that is correlated both in space and time, for instance an instrument
160 bias, is very small and therefore neglected. Under this framework, the propagation of uncertainty
161 fraction (1) is negligible across the spatiotemporal scales considered, the propagation of uncertainty
162 fraction (2) depends upon the size of the domain considered but is negligible at global scale and across
163 most of the regional domains considered in this study, and propagation of fraction (3) accounts for
164 most of the total average uncertainty. Since we cannot know fractions (1), (2) and (3) and (1) and (2)
165 are negligible or small, we assume that (3) represents 100 % of the uncertainty, i.e the grid cell
166 uncertainty is systematic (correlated) in space and random in time, to provide an upper limit on the
167 uncertainty. In addition, we also take into account the sampling uncertainty when temporally
168 averaging over each grid cell using the standard error, i.e., we take the standard deviation divided by
169 the square root of the number of measurements.

170 In practice, when averaging the daily values for every grid cell i over months, seasons, or years,
171 the uncertainty σ'_i is obtained by adding in quadrature the daily uncertainties $\sigma_{N_i}^2$ and dividing by the
172 number of available daily measurements N_i :

$$\sigma'_i = \frac{\sqrt{\sigma_{i,1}^2 + \sigma_{i,2}^2 + \dots + \sigma_{N_i}^2}}{N_i} \text{ (Eq. 1)}$$

173
174



175 In addition, we add in quadrature σ'_i and the standard error SE_i to obtain the total uncertainty of
176 the temporal average σ_i for every grid cell:

177

$$178 \quad \sigma_i = \sqrt{\sigma'^2_i + SE^2_i} \text{ (Eq. 2)}$$

$$179 \quad SE_i = \frac{SD_i}{\sqrt{N_i}} \text{ (Eq. 3)}$$

180

181 where SD_i is the standard deviation of the daily values in grid cell i . The standard error measures how
182 far the sample mean could be from the true population mean.

183 Finally, when spatially averaging globally or regionally, under the assumption that the errors are
184 correlated across space, the overall uncertainty is calculated by averaging σ_i across the N_j grid cells
185 in spatial domain j weighted by the grid cell area fraction with respect to the total area (i.e., grid cell
186 / total area = w_i) with available retrievals:

187

$$188 \quad \sigma_j = \sum_{i=1}^{N_j} w_i * \sigma_i \text{ (Eq.4)}$$

189

190 4. Results

191

192 Our analysis is divided in two main parts. In the first one (Section 4.1) we assess the annual and
193 seasonal climatological DOD maps for nine distinct regions. In the second one (Section 4.2),
194 emphasis is given on the quantification DOD averages along with their monthly and interannual
195 variability fractional contribution to the AOD, from a global to hemispherical level as well as for
196 specific regional domains.

197

198 4.1 Annual and seasonal geographical distributions of DOD

199

200 4.1.1 North Africa, Tropical Atlantic Ocean and Mediterranean

201

202 According to the long-term average map (Fig. 1), the maximum DODs (up to 1.2) are recorded in
203 the Bodélé depression, which is considered the most active individual dust source of the planet
204 (Washington et al., 2003; Koren et al., 2006; Ginoux et al., 2012). Over the area, the prevailing strong
205 winds are intensified further between the Tibesti mountains and the Ennedi ridge (Washington et al.,
206 2009) forming a low-level jet (Washington and Todd, 2005). This dominant wind pattern, affected
207 by the local topography (Washington et al., 2009), acts as the driving force mobilizing mineral
208 particles from arid and erodible soils of the region (Tegen et al., 2006). Under these favorable
209 conditions, dust aerosols are easily uplifted and accumulated in the atmosphere thus causing the very



210 high DODs (> 0.5) observed in the broader area (Chad, Niger). Throughout the year, the high DOD
211 levels are quite persistent exhibiting, however, a seasonal variation with more intense loads recorded
212 during DJF (Fig. S1-i) and MAM (Fig. S1-ii) following the annual cycle of source activation
213 (Washington et al., 2009). The second hotspot in N. Africa is situated between the northern parts of
214 Nigeria and the southern parts of Niger with annual DODs reaching up to 0.7 (Fig. 1) while on
215 seasonal basis vary from 0.4 (SON; Fig. S1-iv) to 0.8 (JJA; Fig. S1-iii). MIDAS DODs match well
216 with those presented by Rajot et al. (2008), who relied on ground-based sunphotometric
217 measurements of AOD obtained at the Banizoumbou AERONET site. Very high DODs are also
218 evident along the coasts of the Gulf of Guinea, which may be unrealistic considering that dust aerosols
219 are mainly transported there and are mixed with anthropogenic and biomass burning (Knippertz et
220 al., 2015). Along this area of high DODs, MERRA-2 also overestimates the dust fraction compared
221 to LIVAS (Gkikas et al., 2021) thus resulting in higher intensities according to the applied
222 methodology (Section 2). Moreover, the temporal availability of DODs in the region is very limited
223 ($< 10\%$; Fig. 8-c in Gkikas et al., 2021), the DOD uncertainty is large and AOD outliers, either realistic
224 or cloud contaminated, can yield exceptional high DODs in this complex environment where aerosol
225 and clouds are spatially correlated (Andrew Sayer, personal communication).

226 Across the Sahara Desert, there is a distinct longitudinal contrast with more intense dust loads in
227 western North Africa than in eastern North Africa (Fig. 1). In the former sector, the DODs range
228 mainly from 0.3 to 0.6 while over the eastern parts of the Sahara the corresponding limits are bounded
229 between 0.1 and 0.3 without revealing significant intra-annual variation. During MAM (Fig. S1-ii),
230 along the southern Sahel, the activation of dust sources results in DODs which locally can exceed
231 0.8, while during boreal summer (Fig. S1-iii) a vast area of the western Sahara is under the impact of
232 heavy dust loadings (DOD > 0.5). According to Ginoux et al. (2012), in the former region, dust is
233 mainly produced by agricultural activities (cultivation, overgrazing) disturbing soils in which alluvial
234 sediments have been accumulated. Northwards, dust has natural origin and the accumulation of
235 mineral particles is favored by the development of the Saharan Heat Low (SHL) affecting also the
236 prevailing airflow (harmattan winds) as well as the West African Monsoon (WAM) (Schepanski et
237 al., 2017). Under these meteorological conditions, several dynamic processes, from mesoscale to
238 microscale, are taking place triggering dust emission (Knippertz and Todd, 2012) from highly active
239 sources (Schepanski et al., 2007).

240 Under the impact of the trade winds, Saharan dust can travel across the tropical Atlantic Ocean
241 reaching the Caribbean Sea, the southern United States and northeastern South America (Prospero,
242 1999; Prospero et al., 2014). The signal of this long-range transport is evident on the annual
243 climatological pattern (Fig. 1) with DODs up to 0.6 (off the western Saharan coasts) fading down to
244 0.1 at the maximum distance. Within the course of the year, the Saharan dust plume varies in terms



245 of intensity, range and latitudinal position, as it is depicted in Figure S1. During boreal summer (Fig.
246 S1-iii), the corridor of the transatlantic dust transport is bounded between 10° N and 20° N latitudes
247 whereas both the intensity (DODs up to 0.6) and the range are maximized. During boreal winter (Fig.
248 S1-i), the dust zone migrates southwards (between Equator and 10° N) while maximum (up to 0.6)
249 and considerable (0.1-0.2) DODs are observed over the Gulf of Guinea and mid-Atlantic (45° W),
250 respectively. Between the transition seasons (Fig. S1-ii, S1-iv), dust loads are stronger in MAM
251 (~0.45), mainly residing within 5° N and 20° N latitudes, in contrast to SON (~0.3) when are shifted
252 northwards (10° N and 25° N). According to the existing literature, several factors modulate the
253 westwards propagation of dust plumes, originating in the western Sahara and the Bodélé Depression,
254 over the tropical Atlantic. For instance, the south-north displacement of the Saharan plumes is driven
255 by the location of the Intertropical Convergence Zone (ITCZ) and the disturbances of the African
256 easterly jet (Knippertz and Todd, 2012; Doherty et al., 2012). Teleconnection patterns, such as the El
257 Niño–Southern Oscillation (ENSO; Prospero and Lamb, 2003), the North Atlantic Oscillation (NAO;
258 Ginoux et al., 2004) and the North African Dipole Index (NAFDI; Rodríguez et al., 2015) have been
259 also studied in order to interpret the decadal variations of dust concentrations over the Atlantic.
260 Likewise, the vegetation coverage across the Sahel as well as the wind speeds, determined by the
261 prevailing atmospheric circulation, over the Sahara play a key role on the amount of the emitted dust
262 particles.

263 Due to the vicinity of the largest deserts of the planet, the Mediterranean is affected by dust
264 outbreaks throughout the year (Gkikas et al., 2013; Marinou et al., 2017). Mineral particles originating
265 primarily from north African and secondarily from Middle Eastern deserts are transported towards
266 the Mediterranean under the prevalence of cyclonic systems (Gkikas et al., 2015). The intensity of
267 dust loads decreases for increasing latitudes, forming a distinct south-north gradient with DODs up
268 to 0.20 between the gulfs of Gabes (Tunisia) and Sidra (Libya), according to the annual pattern (Fig.
269 1). Among seasons (Fig. S1), DODs vary on the locations where the maximum levels are recorded as
270 well as on their magnitude, attributed to the position of the prevailing synoptic systems (Gkikas et
271 al., 2015). The central and eastern Mediterranean sectors are affected by dust loads mainly in spring
272 (DODs up to 0.3; Fig. S1-ii) and winter (DODs up to 0.12; Fig. S1-i). In summer (Fig. S1-iii), dust
273 activity is more pronounced in the western parts with optical depths up to 0.18 (Alboran Sea), while
274 thanks to the fine resolution product, “hotspots” of similar DODs can be identified in the southern
275 parts (Andalucia) of Spain. In SON (Fig. S1-iv), dust loads are found in the central Mediterranean
276 with DODs lower than 0.12 off the Tunisian and Libyan coasts.

277
278
279



280 4.1.2 Middle East

281

282 In the Middle East, there is a zone of moderate-to-high DODs (locally up to 0.8) extending from
283 Mesopotamia to the southern parts of the Saudi Arabia, where one of the largest sand deserts of the
284 world (Rub' al Khali) (Hamidi et al., 2013) is situated (Fig. 2). Based on Ginoux et al. (2012), the
285 origin of mineral particles between Tigris and Euphrates as well as across the Rub' al Khali Desert is
286 mainly natural while in the intermediate part (Ad-Dahna Desert) dust accumulation is attributed to
287 the mixing of anthropogenic and hydrological sources. Slightly higher maximum DODs (up to 0.7;
288 Fig. 2) are recorded in Oman and particularly between Dhofar and Al Wusta, in contrast to previous
289 studies (Pease et al., 1998) which have identified the Wahiba Sands area as a major dust source or the
290 coastal areas of Yemen (Ginoux et al., 2012). On a seasonal basis, the intensity of mineral loads
291 exhibits a strong variability with minimum DODs (up to 0.4) during DJF (Fig. S2-i) and SON (Fig.
292 S2-iv) and maximum (up to 1) during the dry period of the year (Figs S2-ii, S2-iii), being in agreement
293 with the results presented in Yu et al. (2013). More specifically, across the Arabian Peninsula, the
294 increase in DOD levels is getting evident in boreal spring and it is further intensified during summer
295 months. Dust storms emanating in Iraq and the eastern parts of Saudi Arabia favor dust transport
296 towards the Persian Gulf (Gianakopoulou and Toumi, 2012) account for the considerable high DOD
297 levels (>0.6) found there. Due to convergence of the northern-northernwesterly Shamal winds (Yu et
298 al., 2016) and the airflow from the subtropical anticyclone, in JJA, mineral particles are travelling at
299 even longer distances towards the northern Arabian Sea (Ramaswamy et al., 2017), as indicated by
300 the intense dust loads (DODs up to 0.5; Fig. S2-iii) contributing about half of the AOD (Jin et al.,
301 2018). Likewise, during boreal summer, short-range dust transport takes place off the coasts of Oman
302 and Yemen (Gulf of Aden). Among seas in the vicinity of the Arabian Peninsula, the most intense
303 dust loads are observed in the Red Sea, forming a clear latitudinal gradient on annual (Fig. 2) and
304 summer (Fig. S2-iii) geographical DOD patterns, as it has been noted also in Brindley et al. (2015)
305 and Banks et al. (2017). Due to its location, the southern sector of the Red Sea receives dust aerosols
306 either originating from the Republic of Sudan or from the Arabian Peninsula, depending on the zonal
307 airflow (Banks et al., 2017). Dusty air masses travelling westwards are uplifted when they are
308 crossing the mountain range in the southwestern Arabian Peninsula and for this reason dust loads
309 over the southern basin are suspended above 2 km (Banks et al., 2017). On the contrary, low-elevated
310 dust layers are recorded when winds blow from west, triggering dust emission from the Tokar Gap
311 (Sudanese coasts) and subsequently dust outflows into the southern Red Sea (Banks et al., 2017).

312

313

314



315 4.1.3 Central and southwest Asia

316

317 Northwards and eastwards of the Caspian Sea, various deserts are situated in the central segments
318 of the Asian continent. Most part of Turkmenistan is occupied by the Karakum Desert while the
319 Kyzylkum Desert is located in Uzbekistan. Other arid regions stretch between the Caspian and Aral
320 Seas (Ustyurt plateau), in the eastern and southern flanks of the Aral Sea (Solonok Desert) and in the
321 lowlands of western Kazakhstan and southeastern Russia (Ryn Desert) (Elguindi et al., 2016). Based
322 on our seasonal spatial patterns (Fig. S3), the major dust activity is recorded in the Ustyurt Plateau
323 (Li and Sokolik, 2018) and in the large lagoon embayment of Garabogazkol (Shen et al., 2016), a gulf
324 of Turkmenistan dried into a salt-covered playa (Gills, 1996), with minimum (in DJF and SON) and
325 maximum (in MAM and JJA) DODs equal to ~0.2 and ~0.4, respectively. In the rest of areas, the
326 corresponding upper limits can reach up to 0.8-0.9, during boreal summer, in localized spots
327 (Chimboy Lake, Sarygamysh Lake) across the Karakum and Kyzylkum Deserts. For the same season,
328 moderate dust loadings (DOD up to 0.25) are encountered in the southern Caspian Sea (Elguindi et
329 al., 2016) as the result of transported mineral particles mainly coming from the sandy deserts of
330 Turkmenistan (Xi and Sokolik, 2015), under the impact of eastern/southeastern winds (Shen et al.,
331 2016). Since the 1960s, the anthropogenic intervention (agricultural activities, over-irrigation) caused
332 the retreat of the Aral Sea and the formation of the Aralkum Desert (Saiko and Zonn, 2000; Micklin,
333 2007) from which large amounts of aeolian dust are emitted and travel distances of hundreds of
334 kilometers (Indoitu et al., 2015). According to the annual climatological map (Fig. 3), extremely high
335 DODs (> 1) are found in the southeastern parts of the Aralkum Desert (Fig. 3) which are also
336 persistent among the seasons (Fig. S3).

337 In the Sistan basin, extending between Iran-Pakistan-Afghanistan, the long-term average JJA
338 DODs can reach up to 1.1 (Figure S3-iii) in the Margo Desert (Afghanistan), due to the frequent
339 occurrence of dust storms (Middleton, 1996), triggered by the northerly Levar winds, blowing from
340 June to September (Alizadeh Choobari et al., 2014). These maximum DOD levels are substantially
341 higher than the annual mean (0.8; Figure 3) as well as against the corresponding averages for the
342 other seasons. Thanks to the high-resolution MIDAS DOD, we identify the borders of other active
343 arid regions, surrounded by mountain ranges, such as the Rigestan (Afghanistan), the Balochistan
344 (Pakistan), the Dasht-e-Kavir (Iran), the Dasht-e-Lut (Iran) and the Jazmurian drainage basin (Iran).
345 In the aforementioned topographic lows, the magnitude of the dust loads is significantly lower than
346 those observed in the Margo Desert and can be as large as 0.6 (Balochistan) during hot-dry months
347 (Figure S3-iii). The presence of absorbing mineral particles, over the area and in the northernmost
348 part of the Arabian Sea, is also confirmed by the high AI values, especially in June-July, discussed



349 by Rashki et al. (2015), who relied on long-term records obtained by the OMI and TOMS spaceborne
350 sensors.

351

352 4.1.4 Indian subcontinent

353

354 In the Indian subcontinent, the maximum annual DODs (~ 0.5 ; Fig. 4) are observed along the Indus
355 river basin, in the western side of the Thar Desert whereas a branch of gradually decreasing DODs,
356 along the Indo-Gangetic plain towards eastwards directions, is also evident. Ginoux et al. (2012)
357 stated that much of dust activity in the Indus river basin is attributed to the suspension of soil particles
358 originating primarily from agricultural land use and to a lesser extent from the desiccation of
359 ephemeral water bodies. The strong presence of absorbing coarse particles over the area is further
360 supported by the coexistence of considerably high Aerosol Index (AI) values (Alam et al., 2011). As
361 indicated by the seasonal patterns (Fig. S4), the processes regulating the suspended dust loads are
362 highly variable during the year causing a remarkable temporal variability of DOD, which is low (< 0.3)
363 in DJF and SON, moderate in MAM (< 0.5) and maximum in JJA (< 0.8). Similar seasonal variability
364 is evident in the Thar Desert, in agreement with the findings of Proestakis et al. (2018) and Dey and
365 Di Girolamo (2010), who used vertically-resolved (CALIOP) and multi-angle (MISR) satellite
366 retrievals, respectively. Nevertheless, our climatological DODs are higher with respect to the
367 CALIOP corresponding values and the MISR non-spherical AODs, particularly when dust activity
368 over the area is pronounced. During the pre-monsoon season, westerly to northwesterly winds are
369 blowing over the Thar Desert mobilizing dust particles which subsequently are advected towards the
370 Indo-Gangetic basin (Dey et al., 2004; Srivastava et al., 2011). According to our results, between the
371 Haryana state and the eastern parts of the plain, DODs fade down from ~ 0.6 - 0.7 to ~ 0.1 - 0.2 , forming
372 a NW-SE gradient (Figs. S4-ii, S4-iii). Such high DODs are attributed to the eastwards propagation
373 of intense dust storms having a strong signature on the optical, microphysical and radiative properties
374 derived by AERONET stations operating in the region (Prasad et al., 2007a; Prasad et al., 2007b; Eck
375 et al., 2010).

376

377 4.1.5 East Asia and North Pacific Ocean

378

379 Northwards of the Tibetan Plateau is located the Tarim Basin (northwest China) in which one of
380 the largest natural dust source resides, the Taklamakan Desert. This elevated desert area (average
381 elevation 1.1 km) is surrounded by the Pamir Plateau (average elevation 5.5 km) in its west side, by
382 the Kunlun Shan range (average elevation 5.5 km) in its southern flanks and by the Tian Shan range
383 (average elevation 4.8 km) along its northern boundaries while only in its eastern margin the ground



384 elevation is low (Ge et al., 2014). DODs are maximized in spring (Fig. S5-ii) yielding values up to 1
385 along the foothills of the Tian Shan and Kunlun Shan ranges, attributed to the role of the topography
386 on winds strengthening (Ge et al., 2014). Similar values are recorded in JJA (Fig. S5-iii) but the
387 geographical distribution reveals that the highest DODs are less widespread in contrast to spring.
388 Throughout the year, the weaker dust loads are recorded during winter and autumn. Our results are
389 consistent with relevant studies that rely on active and passive satellite retrievals either of pure dust
390 load (Proestakis et al., 2018) or AOD (de Leeuw et al., 2018; Sogacheva et al., 2018).

391 A common feature in the seasonal DOD patterns is the reduction of dust loads' intensity towards
392 the interior parts of the Taklamakan Desert, as it has been also documented by Ge et al. (2014), who
393 utilized MISR retrievals. The high-resolution of the MIDAS DOD dataset provides in detail the
394 spatial information of these geographical patterns. During spring, similar high DODs to those found
395 over the Taklamakan Desert are recorded in the Qaidam Basin (northeast side of the Tibetan Plateau),
396 surrounded by the Atlun, Kunlun, Qilian mountain ranges, attributed to strong downslope winds
397 causing the erosion of soil particles (Rohrmann et al., 2013) and their entrainment into the
398 atmosphere. The intensity of dust loads over the Gobi Desert (north China – south Mongolia) hardly
399 exceeds 0.3 on an annual basis (Fig. 5) while it can reach up to 0.4 during spring (Fig. S5-iii). The
400 remarkable deviations in dust abundance between Taklamakan and Gobi during springtime are
401 interpreted by variations in soil characteristics. More specifically, Taklamakan is composed mainly
402 by fine sand particles in contrast to the rocky soils of the Gobi Desert (Sun et al., 2013). Due to these
403 differences in soil textures, dust particles from the former desert region can be emitted even with low
404 wind speeds while they are uplifted at higher elevations in the troposphere, as it has been shown with
405 MISR stereo observations (Yu et al., 2019) and CALIOP lidar profiles (Proestakis et al., 2018). The
406 injection of Taklamakan dust particles at higher altitudes increase their residence time inducing also
407 their entrainment into the upper-level westerly airflow, around at 4 a.m.s.l., both contributing to the
408 higher potential for long-range transport (Yu et al., 2019), in contrast to Gobi dust, towards the
409 continental E. Asia and the northern Pacific Ocean. Under the impact of cold fronts, propagating
410 eastwards (Eguchi et al., 2009) in spring, air masses carrying mineral particles, during the first two
411 days of dust transport, affect a wide area of China (Yu et al., 2019), from near sources to its eastern
412 parts, through the Hexi Corridor and the Loess Plateau (DODs ranging from 0.2 to 0.4; Fig. S5-iii).
413 Subsequently, the Asian dust plumes are suspended over the Yellow Sea, the Korean Peninsula and
414 further eastwards, in a latitudinal band bounded between the parallels 30°N and 45°, reaching the
415 west coasts of the United States (Yu et al., 2008). Across this “belt”, where the Trans-pacific dust
416 transport is taking place, the springtime DODs decrease smoothly from 0.15 to 0.05 (Fig. S5-ii). In
417 summer (Fig. S5-iii), DODs up to 0.05 are observed between 40° N and 60° N indicating a northwards



418 displacement of the Asian dust layers (mainly originating from the Gobi Desert) due to the weakening
419 and northwards shift of the polar jet streams (Yu et al., 2019).

420

421 *4.1.6 North America*

422

423 Across N. America, the major dust activity is detected in southwest United States and in northwest
424 Mexico with annual and seasonal DODs hardly exceeding 0.15, as illustrated in Figures 6 and S6,
425 respectively. These weak dust load intensities are mainly recorded in the Sonoran and the Mojave
426 Deserts while lower values are found in the Chihuahuan Desert in which isolated spots (e.g. White
427 Sands Desert) become visible thanks to the high-resolution of the MIDAS DOD dataset. Low-to-
428 moderate DODs are evident in the Great Plains with local maxima (exceeding 0.2 in spring; Fig. S6-
429 ii) in the Great Salt Lake Desert and in the surrounding area as well as in the Baja Californian Desert
430 (Mexico; DODs up to 0.14), residing in the western side of the Gulf of California. Our annual spatial
431 distribution of DOD (Fig. 6) is highly consistent with those of frequency of observation (FoO) of
432 DOD (Ginoux et al., 2012; Baddock et al., 2016) and AI given by Prospero et al. (2002). Moreover,
433 the increase of dust loads' concentration in MAM (Fig. S6-ii), has been also documented by Hand et
434 al. (2016) and Tong et al. (2017), both relying on aerosol observations acquired at numerous stations
435 of the Interagency Monitoring of Protected Visual Environments (IMPROVE) network. During
436 springtime, dust emission over the broader area is associated with the transmit of Pacific cold fronts
437 inducing dust-entraining winds as the result of pressure gradient enhancement (Rivera Rivera et al.,
438 2009). The geomorphological soil characteristics are determinant for dust emission with the most
439 prominent natural sources being ephemeral and dry lakes (Baddock et al., 2016) while anthropogenic
440 dust aerosols are mainly emitted in the Great Plains and in the eastern side of the Gulf of California
441 (Ginoux et al., 2012).

442

443 *4.1.7 Australia*

444

445 Earlier studies based on unconstrained numerical simulations (Tanaka and Chiba, 2006; Wagener
446 et al., 2008) have shown that among the desert areas of the S. Hemisphere, the largest contribution of
447 dust particles arises from Australia. However, a more recent assessment (Kok et al., 2021b) in which
448 dust models have been constrained by observations revealed that the emitted dust amounts from S.
449 America are slightly higher than those of Australia. Due to the fairly bright landmasses and the
450 predominance of weak aerosol loadings, there is minimal contrast between surface and atmosphere
451 leading to systematic algorithm uncertainties, which can explain the slightly lower land DODs than
452 those recorded in the surrounding oceanic regions (Fig. 7 and S7). Nevertheless, in the sources as



453 well as in areas affected by dust plumes the atmospheric signal becomes evident. In particular, the
454 highest dust emissions are encountered in the Lake Eyre Basin (LEB; Prospero et al., 2002) composed
455 by ephemeral lakes, alluvial channels, gibber (stone-covered plains), aeolian sand deposits and
456 bedrocks (Bullard et al., 2008). Based on the annual climatological pattern (Fig. 7), DODs can locally
457 exceed 0.2 (in the southern parts) but in general vary between 0.06 and 0.12. From a seasonal
458 perspective (Fig. S7), the highest DODs (mainly up to 0.18 in the Warburton River estuary, few
459 exceedances above 0.4 are found in local spots) are recorded during austral summer (DJF; Fig. S7-i)
460 and spring (SON; Fig. S7-iv). Similar seasonal variation in ground-based sunphotometric
461 observations at nearby sites (Birdsville, Tinga Tingana), with slightly lower AODs, has been reported
462 by Mitchell et al. (2017). Southwards of the LEB, three spots of notable DODs (up to 0.2 in SON;
463 Fig. S7-iv) are identified in the Lakes Gairdner, Torrens and Frome while northeastwards (Lake
464 Yamma Yamma) and northwards (Simpson Desert) from the basin the suspended dust loads exhibit
465 optical depths as large as 0.12 during the driest months of the year. Similar maximum DODs are
466 recorded in the Northern Territory and in the western side of the Great Dividing Range (Queensland)
467 and in contrast to Ginoux et al. (2012) these levels appear in DJF instead of SON. In the southwestern
468 coastal parts of the Australian landmass as well as in Riverina (southeast), during austral spring (Fig.
469 S7-iv) very low DODs are evident associated with anthropogenic dust originating from agricultural
470 activities (Ginoux et al., 2012). Finally, during the same season, weak signals (DODs up to 0.05) of
471 dust transport are revealed over the Tasman and Timor Seas attributed to the eastward movement of
472 cyclonic frontal systems causing the entrainment of mineral particles in air masses that can travel at
473 long distances (Knight et al., 1995; Choobari et al., 2012).

474

475 4.1.8 South Africa

476

477 Dust activity in S. Africa is mainly related with short-range and short-lived plumes (Vickery et
478 al., 2013) that are suspended at low tropospheric altitudes (below 600 hPa) due to the predominance
479 of anticyclonic circulations inhibiting the vertical extension of dust layers (Piketh et al., 1999).
480 Mineral aerosol loadings are mainly originating from the ephemeral lake basins of the Etosha Pans
481 (Namibia) and Makgadikgadi Pans (Botswana) and the Namib Desert (Bryant et al., 2007; Vickery
482 et al., 2013). In the aforementioned source areas, the maximum annual (Figure 8) and seasonal (Figure
483 S8) DODs are equal to 0.1 and 0.16, respectively. Throughout the year, the increase of DODs in
484 Etosha and Makgadikgadi Pans is evident primarily in DJF (Figure S8-i) and secondarily in SON
485 (Figure S8-iv). Our results are consistent with those provided by Ginoux et al. (2012) and Bryant et
486 al. (2007) for the former region (including also the Kalahari Desert in which very weak dust loads are
487 recorded), contradictory for the latter one and opposite with the findings of Vickery et al. (2013) for



488 both sources. In these arid areas dust emission is linked with lakes' inundation, characterized by
489 strong intra-annual variability, playing an important role when different time periods are considered.
490 However, it must be also taken into account the moderate performance of the MERRA-2 dust portion
491 with respect to LIVAS in S. Africa as well as in most desert areas of the S. Hemisphere (Gkikas et
492 al., 2021). Along the Namibian coastline, the deviations of DOD between the high- and low-dust
493 seasons are small indicating that dust activity remains relatively constant within the course of the year
494 (Ginoux et al., 2012). Soil particles from salt pans and dry river beds of the Namib Desert are emitted
495 from aeolian processes related to bergwinds (katabatic winds) blowing in the escarpment, from the
496 Central Plateau down to the coasts (Eckardt and Kuring, 2005). Dust outflow towards the Southern
497 Atlantic Ocean, with a SE-NW orientation, it is shown between 18° S and 9° S during austral winter
498 (DODs up to 0.08; Fig. S8-iii), becoming more evident in SON (Fig. S8-iv), being in agreement with
499 the geographical distributions provided by Voss and Evan (2020). Such transport is favored by the
500 propagation of barotropic low-level easterly waves formed between continental high pressure systems
501 and the semi-permanent South Atlantic anticyclone (Tyson et al., 1996). Finally, weak signals of
502 DODs are recorded in the croplands north of Cape Town, with annual and DJF DODs not exceeding
503 0.1.

504

505 4.1.9 South America

506

507 In South America, the most intense dust loads are encountered in the Patagonia Desert where the
508 most active dust sources are situated in the river basins of the Rio Negro and Chubut provinces and
509 in its southern end. Among these areas, higher DODs (up to 0.16 in DJF; Figure S9-i) are found along
510 the Rio Negro attributed to anthropogenic dust originating from overgrazing, irrigation and oil
511 prospecting (McConnell, et al., 2007; Mazzonia and Vazquez, 2009). In southern latitudes, mineral
512 particles originate from glacier washout plains (Hernández et al., 2008). Under favorable
513 meteorological conditions, aeolian dust from Patagonia travels either towards the southern Atlantic
514 Ocean, contributing to iron concentrations and marine biological productivity in the surface waters
515 (Johnson et al., 2011), or towards the Antarctica peninsula (Gassó et al., 2010), as it has been found
516 in ice core samples (Basile et al., 1997). Both transport pathways are not visible in our climatological
517 patterns (Figures 9 and S9) since dust outbreaks are not so strong (Foth et al., 2019) while the
518 extended cloud coverage over the region results in large observational gaps of the spaceborne
519 retrievals (Gassó and Torres, 2019). Along the western side of Andes, dust emission arises from
520 natural sources located in the Sechura (Peru), Nazca (Peru) and Atacama (Chile) Deserts (Ginoux et
521 al., 2012). In the aforementioned regions, the annual DODs (Figure 9) can reach up to 0.1, 0.08 and
522 0.06, respectively, while the intra-annual variability is characterized weak (Figure S9). During MAM



523 (Figure S9-ii), DODs up to 0.16 appear in Guyana, Suriname and French Guiana as well as over their
524 offshore areas while similar intensities are evident in the northern parts of the Amazon rainforest
525 (around the Equator and bounded between 65°W and 60°W). The presence of coarse mineral particles
526 (Moran-Zuloaga, et al., 2018) over these distant areas from deserts, is attributed to the long-range
527 dust transport from North Africa across the Atlantic Ocean (Yu et al., 2015), under the impact of the
528 trade winds, taking place northwards of the convective precipitation zone formed around the ITCZ.
529 Finally, the latitudinal zone of weak DODs in the western parts of Brazil, fading down abruptly
530 eastwards of ~58° W, indicates an artifact of the MIDAS product that becomes more evident in SON
531 (Fig. S9-iv). This peculiar pattern is induced by the MERRA-2 dust fraction (results not shown here)
532 which is used for the derivation of MIDAS DOD from the MODIS AOD. An additional deficiency is
533 the relatively large DODs over an area where biomass burning particles, emitted at enormous amounts
534 by extended wildfires, clearly dominate over other aerosol species. Under these conditions, the non-
535 dust AODs are very high as well as their relevant uncertainties (Eqs. 5-7 in Gkikas et al. (2021)) while
536 the reliability of the MERRA-2 dust fraction downgrades there (see Fig. 2 in Gkikas et al. (2021)).

537

538 *4.2 DOD averages and variability at global, hemispherical and regional scales*

539

540 In this section, we discuss the average AOD and DOD along with their monthly and interannual
541 variability at global, hemispherical and regional scales. The left column of Figure 10 shows the
542 interannual timeseries of AOD (black curve) and DOD (red curve) averaged over the whole globe
543 (upper panel; GLB), the Northern Hemisphere (middle panel; NHE) and the Southern Hemisphere
544 (bottom panel; SHE). The right column of Figure 10 depicts the monthly seasonal cycle of AOD and
545 DOD along with the DOD-to-AOD ratio (blue curve) while the shaded areas correspond to the total
546 uncertainty.

547 The significant role of dust particles in the global aerosol budget becomes evident by visually
548 inspecting the AOD and DOD interannual timeseries (Fig. 10 i-a). The monthly contribution of
549 suspended dust to the total AOD varies from 14% to 39%, with minimum values mainly in DJF and
550 maximum values in MAM or JJA depending on the year. Monthly DODs range from 0.016 ± 0.013
551 (Dec 2005) to 0.063 ± 0.028 (Mar 2012), whereas the long-term global annual average is equal to
552 0.032 ± 0.003 (Table 1). The global DOD mean, computed here from the fine resolution data, is
553 almost identical with those obtained by the coarse spatial resolution MERRA-2 and MIDAS DODs
554 and slightly higher than those calculated based on LIVAS-CALIOP (0.029) (see Table 1 in Gkikas et
555 al. (2021); it is noted the three datasets they had been collocated). Likewise, our global average and
556 uncertainty computed over the period 2004–2008 (0.033 ± 0.004) is close to the one obtained in Ridley
557 et al. (2016) (0.030 ± 0.005), despite the different methods applied for the derivation of DOD and its



558 uncertainty. Our global DOD long-term average is very close to the CALIOP derived value (0.029)
559 and about half of the MODIS derived one (0.063) reported by Song et al. (2021).

560 Our continental (0.070 ± 0.005) and oceanic (0.019 ± 0.002) mean DODs (see Table 1) are
561 substantially lower than those obtained in Voss and Evan (2020) (land: 0.1; ocean: 0.03). This
562 difference may be attributed to the different averaging approaches, which can have an important
563 impact on the calculations as it has been shown in Levy et al. (2009) (see their Figure 5). Based on
564 our method, we are giving the same “weight” at each grid cell (regardless of the amount of available
565 data in that grid cell throughout the study period) when we are calculating the domain (from regional
566 to global) average. Therefore, we are avoiding an overestimation of the spatial average since MIDAS
567 data availability is larger over/nearby deserts (see Figure 8-c in Gkikas et al. (2021)) where the higher
568 DODs are observed. To be more specific, when we are calculating the global long-term DOD average
569 based on the second branch (i.e., “Straight”, the standard approach for the calculation of the average
570 value by considering all the available values in space and time) in Levy et al. (2009), we obtain a
571 climatological value equal to 0.047. Such different approaches for the calculation of the long-term
572 DOD averages might interpret and the deviations found between this study and Song et al. (2021).
573 Finally, the computed global mean MIDAS DOD is somewhat higher than those simulated by most
574 AeroCom Phase I models (Huneeus et al., 2011), being about 40% higher than the median (0.023);
575 nevertheless, it must be taken into account that most models account for the diurnal variation of DOD
576 in contrast to the single-measurements taken during MODIS overpass.

577 As expected, the interannual GLB DOD timeseries is driven by the variability in the NHE DOD
578 (Figure 10 ii-a) since the most widespread and intense dust sources are located in the Northern
579 Hemisphere. This is justified by their high temporal co-variation while a positive NHE-GLB offset is
580 constantly observed, being lower during boreal winter and autumn (up to 0.035) and maximum during
581 the high dust seasons (0.058). The fraction of monthly NHE AOD attributed to dust particles ranges
582 from 20% to 48% and the R^2 value between monthly AOD and DOD is equal to 0.94, both indicating
583 a dominant dust contribution. Over the study period (2003-2017), the NHE DOD yields a
584 climatological mean equal to 0.056 ± 0.004 (Table 1) ranging from 0.024 ± 0.015 (Dec 2005) to 0.121
585 ± 0.050 (Mar 2012). In contrast, marine and biomass burning aerosols, rather than dust, regulate AOD
586 in the Southern Hemisphere (Figure 10 iii-a). SHE DODs are estimated to be low (0.008 ± 0.001),
587 with the maximum value (0.016 ± 0.016) recorded in February 2016. The contribution of dust aerosols
588 to the total aerosol load does not exceed 17% throughout the study period (Fig. 10 iii-a) and on
589 average it is equal to $8.2\% \pm 1.1\%$, which is in very good agreement with the findings by Kok et al.
590 (2021b).

591 A better view of the seasonal cycles of AOD, DOD and the DOD-to-AOD ratio can be obtained
592 by investigating their climatological patterns, representative for the period of interest (2003-2017).



593 On a global scale (Fig. 10 i-b), DODs peak between March and June (~0.045), and then decline until
594 November (0.018) before rising during boreal winter. Despite the monthly shifts between maximum
595 AOD and DOD averages, the seasonal cycles of the total aerosol and dust burdens are similar to a
596 large extent, whereas the contribution of mineral particles to the total extinction ranges from 16%
597 (November) to 33% (March-June). The MIDAS global DOD-to-AOD ratio (~23%) is close to the
598 values reported by Gelaro et al. (2017) and Kinne et al. (2006), ~22% and ~26%, respectively, but
599 higher than most of the model-derived estimations (12% - 28%) from the AeroCom Phase III (Gliss
600 et al., 2021). These discrepancies, excluding the aerosol parametrizations, may be partly due to the
601 different sampling between single-overpass satellite observations and reanalyses (Gelaro et al., 2017)
602 or models (Kinne et al., 2006) where the diurnal aerosol variability (Schepanski et al., 2009; Yu et
603 al., 2021) is included. In the NHE (Fig. 10 ii-b), the mean seasonal trend of DODs remains relatively
604 unchanged when compared with GLB; however, the hemispheric means (0.030-0.088) and the dust
605 fraction (24-41%) are higher. On the contrary, the weak signal of aeolian dust in SHE (Fig. 10 iii-b)
606 interprets the very low DODs (0.005 – 0.011) and their minor impact (6-12%) upon AOD magnitude.

607 The analysis presented above has also been conducted for each one of the 17 sub-regions
608 illustrated in Figure 7 in Gkikas et al. (2021), and the main findings are summarized in this paragraph.
609 Among the regional domains, a persistency of high DODs (>0.3), both at interannual and seasonal
610 scales, it is found only in BOD, which yields a long-term average value equal to 0.533 ± 0.009 , being
611 almost double than WSA (0.302 ± 0.006) and TAK (0.246 ± 0.020) as illustrated in Table 1. However,
612 when focus is given to individual months, the maximum DODs over the study period (Fig. 11 vi-a)
613 and on their climatological levels are recorded in the Taklamakan Desert and can be as high as 0.868
614 (April 2007) and 0.600 (April), respectively. Comparable or even higher DODs than those computed
615 in BOD, are also evident for specific months in THA (Fig. 11 vii-a), GOG (Fig. 11 xii-a) and SSA
616 (Fig. 11 xv-a) as well as on the monthly timeseries (THA; Fig. 11 vii-b). Mineral particles'
617 contribution to the total AOD (i.e., blue curves in the seasonal cycle plots) is at least 50% over dust
618 sources or dust-abundant areas in N. Africa, Middle East and Asia and it is constantly higher than
619 70%, reaching up to 95%, in BOD (Fig. 11 i-b), WSA (Fig. 11 viii-b) and TAK (Fig. 11 vi-b). Over
620 downwind regions, such as EAS (Fig. 11 ix-b), GOG (Fig. 11 xii-b), MED (Fig. 11 xiii-b) and SSA
621 (Fig. 11 xv-b), the dust contribution can prevail over the non-dust portion (GOG, MED, SSA) while
622 in EAS does not exceed 30%, due to the predominance of anthropogenic aerosols. In the oceanic
623 areas of Tropical Atlantic and North Pacific, where large-scale dust transport is taking place, AOD
624 and DOD co-vary, indicating that the dust activity regulates the temporal variations of aerosols' load,
625 except during summer months in WNP (Fig. 11 xvi-a, xvi-b). Regarding the seasonal cycle of DOD,
626 the maximum values are recorded either during boreal spring (GOB, CAS, NME, SUS, TAK, EAS,



627 ENP, GOG, MED, WNP and SSA) or during boreal summer (THA, WSA, ETA, SME and WTA) or
628 are similar between the two high-dust seasons (BOD).

629 A final intercomparison of the MIDAS DODs against those derived by Ridley et al. (2016) and
630 Adebisi et al. (2020), on a seasonal basis over the period 2004 - 2008, has been performed for 15
631 regions defined in Kok et al. (2021a) (see their Figure 2-b and Table 2). The obtained results are
632 illustrated in Figure 12. For the southern hemisphere regions (Figs. 12 –xiii, xiv, xv) as well as for
633 North America (Fig. 12-xii), MIDAS DODs are compared versus those from Adebisi et al. (2020)
634 while for the remaining 11 domains (Figs. 12-i – xi) the results from Ridley et al. (2016) have been
635 utilized. As an overview, it is noted that the seasonal cycle among the three databases is commonly
636 reproduced, with a few exceptions (Mali-Niger, Kyzyl Kum, Southern Africa), whereas the DOD
637 uncertainties (represented by the error bars) are comparable. Regarding the magnitudes, MIDAS
638 DODs are mainly somewhat lower than those of Ridley et al. (2016) across the dust belt in contrast
639 to the outflow region of the Mid-Atlantic (Fig. 12-i). The obtained differences are mainly attributed
640 to the consideration of different models for accounting for the non-dust portion, the different
641 treatment of AODs (bias correction vs. quality filtering), the different versions of MODIS retrievals
642 (C006 vs C061), the consideration of multi-satellite observations instead of relying only on MODIS-
643 Aqua retrievals as well as to the different spatial scales (coarse vs. fine). In relative terms, the largest
644 deviations are found in the desert areas of the southern hemisphere where models struggle to represent
645 adequately the dust sources and the emitted amounts of mineral particles, thus affecting the dust
646 fraction ratio.

647

648 **5. Summary and conclusions**

649

650 The current study presents the first scientific exploitation of the MIDAS dataset (Gkikas et al.,
651 2021), which provides columnar mid-visible (550 nm) dust optical depth (DOD) at fine spatial
652 resolution ($0.1^\circ \times 0.1^\circ$) and over a 15-year period (2003 – 2017). Taking advantage of the global
653 coverage of the MIDAS DOD product, we analyzed the contribution of dust aerosols to AOD at
654 various spatial and temporal scales. More specifically, we focused on 9 regions that account for the
655 majority of the global dust budget, including sources and downwind areas with the main dust transport
656 pathways. Such regions comprise the deserts extending across the “dust belt”, North America,
657 Australia, South Africa and South America as well as maritime areas (Tropical Atlantic Ocean,
658 Mediterranean, North Pacific Ocean) receiving constantly large amounts of mineral particles from
659 the nearby deserts. At a further step, the interannual and intra-annual timeseries of DODs along with
660 their contribution to the total aerosol load (AOD), were investigated at global, hemispherical and
661 regional level.



662 According to our findings, the global long-term DOD average over the study period (2003-2017)
663 is equal to 0.032 ± 0.003 , yielding a strong contrast between the contributions from the northern
664 (0.056 ± 0.004) and southern (0.008 ± 0.001) hemispheres. Our global estimations are almost identical
665 with those given by Ridley et al. (2016) and the CALIOP-derived estimate of Song et al. (2021), in
666 contrast to the MODIS-based given from the latter study. Nevertheless, when the global averages are
667 calculated separately over land (0.070 ± 0.005) and ocean (0.019 ± 0.002), our results differ
668 substantially than those found in Voss and Evan (2020), who reported continental and maritime DODs
669 equal to 0.100 and 0.030, respectively. The large deviations found with the latter study are attributed
670 to the different applied methodologies and averaging procedures followed. Moreover, we find very
671 good agreement, in terms of DOD magnitude and uncertainty, of the MIDAS seasonal DODs versus
672 those of Ridley et al. (2016) and Adebisi et al. (2020) for 15 regions defined in Kok et al. (2021a).
673 Considering that the long-term DOD averages can be utilized for constraining global dust in climate
674 models, or can be used in several other applications, a detailed analysis is required for enlightening
675 the factors resulting in disagreements among studies. Likewise, our computed global DOD average
676 resides around the middle of the AeroCom (Huneeus et al., 2011) limits, being higher than the median
677 (0.023) and mean (0.028). However, in the model-based calculations the diurnal variability is taken
678 into account in contrast to the satellite-based estimations relying on single overpass measurements
679 per day.

680 Regarding the dust contribution to the total aerosol optical depth, the DOD-to-AOD ratio from
681 32% at N. Hemisphere drops down to 8% in S. Hemisphere while at global scale is about one quarter
682 (23%). The contradiction found between the two hemispheres, both for DOD and dust fraction, is
683 interpreted by the most pronounced dust activity recorded in the Bodélé Depression of the northern
684 Lake Chad Basin (DODs up to ~ 1.2), across the Sahel (DODs up to 0.8), in western parts of the
685 Sahara Desert (DODs up to 0.6), in the eastern parts of the Arabian Peninsula (DODs up to ~ 1), along
686 the Indus river basin (DODs up to 0.8) and in the Taklamakan Desert (DODs up to ~ 1). On the
687 contrary, the weaker emission mechanisms triggering dust mobilization over the spatially limited
688 sources of Patagonia, South Africa and interior arid areas of Australia do not favor the accumulation
689 of mineral particles at large amounts (DODs up to 0.4 at local hotspots), even during high-dust
690 seasons. Except for the Bodélé Depression, where the seasonal variability of the intense dust loads is
691 relatively weak, in the other dust sources of the N. Hemisphere, DODs exhibit a strong seasonal cycle
692 with maximum levels either during boreal spring or summer and minimum in boreal winter.

693 Over oceans, the main pathways of long-range dust transport are observed along the tropical
694 Atlantic and the northern Pacific, revealing a remarkable variation, within the course of the year, in
695 terms of intensity, latitudinal position and range. Saharan dust plumes, reaching the Caribbean Sea in
696 summer under the impact of the trade winds, are more abundant with respect to Asian dust, arriving



697 at the western coasts of the United States in spring under the impact of midlatitude cyclones. Due to
698 the convergence of the Shamal winds, blowing over the Arabian Peninsula, and the wind flow from
699 the subtropical anticyclone, dust aerosols originating in the Middle East can reach the western Indian
700 coasts in summer, crossing the Arabian Sea. Dust loads in the southern parts of the Red Sea are
701 maximized during boreal summer when Saharan or Middle East dust is transported, depending on the
702 zonal airflow. The intensity of dust burden in the Mediterranean forms a south-north gradient,
703 whereas a seasonal longitudinal shift of the maximum DODs, off the northern African coasts, is
704 evident attributed to the prevailing synoptic circulation.

705 The performed analysis here can serve as the basis of a follow-up study in which emphasis will
706 be given on DOD trends, from grid cell to global scale, in order to identify potential variations of
707 mineral atmospheric burden by exploring the temporal availability of the MIDAS dataset. It is
708 expected that thanks to the fine resolution of the MIDAS DOD it will be possible to investigate
709 alterations, throughout the time, of the emitted amounts at the sources and modifications of dust
710 transport patterns and subsequently assess the impact of the contributor mechanisms. Also, we have
711 provided a simple, yet flexible method (independent from other datasets) to calculate consistent
712 uncertainties across spatiotemporal scales, which will ease the use of the MIDAS dataset in future
713 studies (e.g. data assimilation).

714

715 **Acknowledgments**

716 Antonis Gkikas acknowledges support by the Hellenic Foundation for Research and Innovation
717 (H.F.R.I.) under the “2nd Call for H.F.R.I. Research Projects to support Post-Doctoral Researchers”
718 (Project Acronym: ATLANTAS, Project Number: 544). Vassilis Amiridis acknowledges support
719 from the European Research Council (grant no. 725698; D-TECT). Eleni Marinou was funded by a
720 DLR VO-Ryoung investigator group and the Deutscher Akademischer Austauschdienst (grant no.
721 57370121). Jasper F. Kok acknowledges support from National Science Foundation (NSF) grant
722 1552519. Carlos Pérez García-Pando acknowledges support from the European Research Council
723 (grant no. 773051; FRAGMENT), the AXA Research Fund, and the Spanish Ministry of Science,
724 Innovation and Universities (grant nos. RYC-2015-18690 and CGL2017- 88911-R). The authors
725 acknowledge support from the DustClim project as part of ERA4CS, an ERA-NET project initiated
726 by JPI Climate and funded by FORMAS (SE), DLR (DE), BMWFW (AT), IFD (DK), MINECO
727 (ES), and ANR (FR), with cofunding by the European Union (grant no. 690462). PRACE (Partnership
728 for Advanced Computing in Europe) and RES (Red Española de Supercomputación) are
729 acknowledged for awarding access to the MareNostrum Supercomputer in the Barcelona
730 Supercomputing Center. We acknowledge support of this work by the PANhellenic infrastructure for
731 Atmospheric Composition and climatE chAnge (PANACEA) project (grant no. MIS 5021516),



732 which is implemented under the Horizon 2020 Action of “Reinforcement of the Research and
733 Innovation Infrastructure”, funded by the Operational Programme Competitiveness,
734 Entrepreneurship, and Innovation (NSRF 2014–2020) and cofinanced by Greece and the European
735 Union (under the European Regional Development Fund). NOA members acknowledge support from
736 the Stavros Niarchos Foundation (SNF). The authors acknowledge support by the COST Action
737 “InDust” (grant no. CA16202), supported by COST (European Cooperation in Science and
738 Technology). The authors would like to thank Andrew Mark Sayer for his valuable and constructive
739 comments. The authors would like also to thank Thanasis Georgiou for developing the ftp server on
740 which the MIDAS data set is stored.

741

742 **Data availability**

743

744 The MIDAS dataset has been developed in the framework of the DUST-GLASS project (grant no.
745 749461; European Union’s Horizon 2020 Research and Innovation programme under the Marie
746 Skłodowska-Curie Actions) and it is available at: <https://doi.org/10.5281/zenodo.4244106>.

747

748 **References**

749 Adebisi, A. A., Kok, J. F., Wang, Y., Ito, A., Ridley, D. A., Nabat, P., and Zhao, C.: Dust Constraints
750 from joint Observational-Modelling-experimental analysis (DustCOMM): comparison with
751 measurements and model simulations, *Atmos. Chem. Phys.*, 20, 829–863,
752 <https://doi.org/10.5194/acp-20-829-2020>, 2020.

753 Alam, K., Qureshi, S., & Blaschke, T.: Monitoring spatio-temporal aerosol patterns over Pakistan
754 based on MODIS, TOMS and MISR satellite data and a HYSPLIT model. *Atmospheric Environment*,
755 45, 4641–4651, 2011.

756 Alizadeh-Choobari, O., Zavar-Reza, P., Sturman, A.: The “wind of 120 days” and dust storm activity
757 over the Sistan Basin, *Atmos. Res.*, 143, 328–341, 2014.

758

759 Amiridis, V., Wandinger, U., Marinou, E., Giannakaki, E., Tsekeri, A., Basart, S., Kazadzis, S.,
760 Gkikas, A., Taylor, M., Baldasano, J., and Ansmann, A.: Optimizing CALIPSO Saharan dust
761 retrievals, *Atmos. Chem. Phys.*, 13, 12089–12106, <https://doi.org/10.5194/acp-13-12089-2013>, 2013.

762

763 Amiridis, V., Marinou, E., Tsekeri, A., Wandinger, U., Schwarz, A., Giannakaki, E., Mamouri, R.,
764 Kokkalis, P., Biniotoglou, I., Solomos, S., Herekakis, T., Kazadzis, S., Gerasopoulos, E., Proestakis,
765 E., Kottas, M., Balis, D., Papayannis, A., Kontoes, C., Kourtidis, K., Papagiannopoulos, N., Mona,



- 766 L., Pappalardo, G., Le Rille, O., and Ansmann, A.: LIVAS: a 3-D multi-wavelength aerosol/cloud
767 database based on CALIPSO and EARLINET, *Atmos. Chem. Phys.*, 15, 7127-7153,
768 <https://doi.org/10.5194/acp-15-7127-2015>, 2015.
769
- 770 Baddock, M. C., Ginoux, P., Bullard, J. E., and Gill, T. E.: Do MODIS-defined dust sources have a
771 geomorphological signature?, *Geophys. Res. Lett.*, 43, GL067327, doi:10.1002/2015GL067327,
772 2016.
773
- 774 Banks, J. R., Brindley, H. E., Stenchikov, G., and Schepanski, K.: Satellite retrievals of dust aerosol
775 over the Red Sea and the Persian Gulf (2005–2015), *Atmos. Chem. Phys.*, 17, 3987-4003,
776 <https://doi.org/10.5194/acp-17-3987-2017>, 2017.
777
- 778 Basile, I., Grousset, F. E., Revel, M., Petit, J.-R., Biscaye, P. E., and Barkov, N. I.: Patagonian origin
779 of glacial dust deposited in East Antarctica (Vostok and Dome C) during glacial stages 2, 4 and 6,
780 *Earth Planet. Sc. Lett.*, 146, 573–589, 1997.
781
- 782 Brindley, H., Osipov, S., Bantges, R., Smirnov, A., Banks, J., Levy, R., Jish Prakash, P., and
783 Stenchikov, G.: An assessment of the quality of aerosol retrievals over the Red Sea and evaluation of
784 the climatological cloud-free dust direct radiative effect in the region, *J. Geophys. Res.-Atmos.*, 120,
785 10862–10878, doi:10.1002/2015JD023282, 2015.
786
- 787 Bryant, R. G., Bigg, G. R., Mahowald, N. M., Eckardt, F. D., and Ross S. G.: Dust emission response
788 to climate in southern Africa, *J. Geophys. Res.*, 112, D09207, doi:10.1029/2005JD007025, 2007.
789
- 790 Bullard, J. E., and Austin, M. J.: Dust generation on a proglacial floodplain, West Greenland. *Aeolian*
791 *Res.* 3, 43–54. doi: 10.1016/j.aeolia.2011.01.002, 2011, 2017.
792
- 793 Bullard, J. E., Baddock, M., Bradwell, T., Crusius, J., Darlington, E., Gaiero, D., Gassó, S.,
794 Gisladottir, G., Hodgkins, R., McCulloch, R., McKenna-Neuman, C., Mockford, T., Stewart, H., and
795 Thorsteinsson, T.: High-latitude dust in the Earth system, *Rev. Geophys.*, 54, 447–485,
796 <https://doi.org/10.1002/2016RG000518>, 2016.
797
- 798 Bullard, J., Baddock, M., McTainsh, G. H., and Leys, J. F.: Subbasin scale dust source
799 geomorphology detected using MODIS, *Geophys. Res. Lett.*, 35, L15404,
800 doi:10.1029/2008GL033928, 2008.



- 801 Chin, M., Ginoux, P., Kinne, S., Torres, O., Holben, B. N., Duncan, D. N., Martin, R. V., Logan, J.
802 A., Higurashi, H., and Nakajima, T.: Tropospheric aerosol optical thickness from the GOCART
803 model and comparisons with satellite and Sun photometer measurements, *J. Atmos. Sci.*, 59, 451–
804 483, [https://doi.org/10.1175/1520-0469\(2002\)059<0461:TAOTFT>2.0.CO;2](https://doi.org/10.1175/1520-0469(2002)059<0461:TAOTFT>2.0.CO;2), 2002.
- 805
- 806 de Leeuw, G., Sogacheva, L., Rodriguez, E., Kourtidis, K., Georgoulas, A. K., Alexandri, G.,
807 Amiridis, V., Proestakis, E., Marinou, E., Xue, Y., and van der A, R.: Two decades of satellite
808 observations of AOD over mainland China using ATSR-2, AATSR and MODIS/Terra: data set
809 evaluation and large-scale patterns, *Atmos. Chem. Phys.*, 18, 1573-1592, [https://doi.org/10.5194/acp-](https://doi.org/10.5194/acp-18-1573-2018)
810 18-1573-2018, 2018.
- 811
- 812 Dey, S. and Di Girolamo, L.: A climatology of aerosol optical and microphysical properties over the
813 Indian subcontinent from 9 years (2000–2008) of Multiangle Imaging Spectroradiometer (MISR)
814 data, *J. Geophys. Res.-Atmos.*, 115, D15204, <https://doi.org/10.1029/2009JD013395>, 2010.
- 815
- 816 Dey, S., Tripathi, S. N., Singh, R. P., and Holben, B. N.: Influence of dust storms on the aerosol
817 optical properties over the Indo-Gangetic basin, *J. Geophys. Res.-Atmos.*, 109, 1–10,
818 doi:10.1029/2004jd004924, 2004.
- 819
- 820 Di Tomaso, E., Schutgens, N. A. J., Jorba, O., and Pérez García-Pando, C.: Assimilation of MODIS
821 Dark Target and Deep Blue observations in the dust aerosol component of NMMB-MONARCH
822 version 1.0, *Geosci. Model Dev.*, 10, 1107-1129, <https://doi.org/10.5194/gmd-10-1107-2017>, 2017.
- 823
- 824 Doherty, O. M., Riemer, N., and Hameed, S.: Control of Saharan mineral dust transport to Barbados
825 in winter by the Intertropical Convergence Zone over West Africa: Winter dust in Barbados and the
826 ITCZ, *J. Geophys. Res.-Atmos.*, 117, D19117, doi:10.1029/2012JD017767, 2012.
- 827
- 828 Du, Y., Xu, X., Chu, M., Guo, Y., and Wang, J.: Air particulate matter and cardiovascular disease:
829 the epidemiological, biomedical and clinical evidence, *J. Thorac. Dis.*, 8, E8,
830 <https://doi.org/10.3978/j.issn.2072-1439.2015.11.37>, 2016.
- 831
- 832 Eck, T. F., Holben, B. N., Sinyuk, A., Pinker, R. T., Goloub, P., Chen, H., Chatenet, B., Li, Z., Singh,
833 R. P., and Tripathi, S. N.: Climatological aspects of the optical properties of fine/coarse mode aerosol
834 mixtures, *J. Geophys. Res.-Atmos.*, 115, 19205, <https://doi.org/10.1029/2010JD014002>, 2010.
- 835



- 836 Eckardt, F.D. Kuring, N.: SeaWiFS identifies dust sources in the Namib Desert. *International Journal*
837 *of Remote Sensing*, 26:4159–4167, 2005.
- 838
- 839 Eguchi, K., Uno, I., Yumimoto, K., Takemura, T., Shimizu, A., Sugimoto, N., and Liu, Z.: Trans-
840 *pacific dust transport: integrated analysis of NASA/CALIPSO and a global aerosol transport model*,
841 *Atmos. Chem. Phys.*, 9, 3137–3145, <https://doi.org/10.5194/acp-9-3137-2009>, 2009.
- 842
- 843 Elguindi, N., Solmon, F., Turuncoglu, U.: Quantifying some of the impacts of dust and other aerosol
844 *on the Caspian Sea region using a regional climate model*. *Clim. Dyn.*, 46, 41–55, 2016.
- 845
- 846 Fiedler, S., Schepanski, K., Heinold, B., Knippertz, P., and Tegen, I.: Climatology of nocturnal low-
847 *level jets over North Africa and implications for modeling mineral dust emission*, *J. Geophys. Res.-*
848 *Atmos.*, 118, 6100–6121, 2013.
- 849
- 850 Flaounas, E., Kotroni, V., Lagouvardos, K., Kazadzis, S., Gkikas, A., and Hatzianastassiou, N.:
851 *Cyclone contribution to dust transport over the Mediterranean region*, *Atmos. Sci. Lett.*, 16, 473–478,
852 [doi:10.1002/asl.584](https://doi.org/10.1002/asl.584), 2015.
- 853
- 854 Foth, A., Kanitz, T., Engelmann, R., Baars, H., Radenz, M., Seifert, P., Barja, B., Fromm, M.,
855 *Kalesse, H., and Ansmann, A.: Vertical aerosol distribution in the southern hemispheric midlatitudes*
856 *as observed with lidar in Punta Arenas, Chile (53.2° S and 70.9° W), during ALPACA*, *Atmos. Chem.*
857 *Phys.*, 19, 6217–6233, <https://doi.org/10.5194/acp-19-6217-2019>, 2019.
- 858
- 859 Gassó, S., Stein, A., Marino, F., Castellano, E., Udasti, R., and Ceratto, J.: A combined observational
860 *and modeling approach to study modern dust transport from the Patagonia desert to East Antarctica*,
861 *Atmos. Chem. Phys.*, 10, 8287–8303, <https://doi.org/10.5194/acp-10-8287-2010>, 2010.
- 862
- 863 Gassó, S., & Torres, O.: Temporal characterization of dust activity in the Central Patagonia desert
864 *(years 1964–2017)*, *Journal of Geophysical Research: Atmospheres*, 124, 3417– 3434.
865 <https://doi.org/10.1029/2018JD030209>, 2019.
- 866
- 867 Ge, J. M., Huang, J. P., Xu, C. P., Qi, Y. L., and Liu, H. Y.: Characteristics of Taklimakan dust
868 *emission and distribution: a satellite and reanalysis field perspective*, *J. Geophys. Res.-Atmos.*, 119,
869 11772–11783, <https://doi.org/10.1002/2014JD022280>, 2014.
- 870



- 871 Gelaro, R., McCarty, W., Suárez, M. J., Todling, R., Molod, A., Takacs, L., Randles, C. A., Darmenov,
872 A., Bosilovich, M. G., Reichle, R., Wargan, K., Coy, L., Cullather, R., Draper, C., Akella, S.,
873 Buchard, V., Conaty, A., da Silva, A. M., Gu, W., Kim, G., Koster, R., Lucchesi, R., Merkova, D.,
874 Nielsen, J. E., Partyka, G., Pawson, S., Putman, W., Rienecker, M., Schubert, S. D., Sienkiewicz, M.,
875 and Zhao, B.: The Modern-Era Retrospective Analysis for Research and Applications, Version 2
876 (MERRA-2), *J. Climate*, 30, 5419–5454, <https://doi.org/10.1175/JCLI-D-16-0758.1>, 2017.
- 877
- 878 Gill, T. E.: Eolian sediments generated by anthropogenic disturbance of playas: human impacts on
879 the geomorphic system and geomorphic impacts on the human system, *Geomorphology*, 17, 207–
880 228, 1996.
- 881
- 882 Ginoux, P., Prospero, J. M., Torres, O., and Chin, M.: Longterm simulation of global dust distribution
883 with the GOCART model: correlation with North Atlantic Oscillation, *Environ. Modell. Softw.*, 19,
884 113–128, [https://doi.org/10.1016/S1364-8152\(03\)00114-2](https://doi.org/10.1016/S1364-8152(03)00114-2), 2004.
- 885
- 886 Ginoux, P., Prospero, J. M., Gill, T. E., Hsu, N. C., and Zhao, M.: Global-scale attribution of
887 anthropogenic and natural dust sources and their emission rates based on MODIS Deep Blue aerosol
888 products, *Rev. Geophys.*, 50, RG3005, <https://doi.org/10.1029/2012RG000388>, 2012.
- 889
- 890 Gkikas, A., Hatzianastassiou, N., Mihalopoulos, N., Katsoulis, V., Kazadzis, S., Pey, J., Querol, X.,
891 and Torres, O.: The regime of intense desert dust episodes in the Mediterranean based on
892 contemporary satellite observations and ground measurements, *Atmos. Chem. Phys.*, 13, 12135–
893 12154, <https://doi.org/10.5194/acp-13-12135-2013>, 2013.
- 894
- 895 Gkikas, A., Houssos, E. E., Lolis, C. J., Bartzokas, A., Mihalopoulos, N., and Hatzianastassiou, N.:
896 Atmospheric circulation evolution related to desert-dust episodes over the Mediterranean, *Q. J. Roy.
897 Meteor. Soc.*, 141, 1634–1645, doi:10.1002/qj.2466, 2015.
- 898
- 899 Gkikas, A., Basart, S., Hatzianastassiou, N., Marinou, E., Amiridis, V., Kazadzis, S., Pey, J., Querol,
900 X., Jorba, O., Gassó, S., and Baldasano, J. M.: Mediterranean intense desert dust outbreaks and their
901 vertical structure based on remote sensing data, *Atmos. Chem. Phys.*, 16, 8609–8642,
902 <https://doi.org/10.5194/acp-16-8609-2016>, 2016.
- 903
- 904 Gkikas, A., Obiso, V., Pérez García-Pando, C., Jorba, O., Hatzianastassiou, N., Vendrell, L., Basart,
905 S., Solomos, S., Gassó, S., and Baldasano, J. M.: Direct radiative effects during intense Mediterranean



- 906 desert dust outbreaks, *Atmos. Chem. Phys.*, 18, 8757–8787, <https://doi.org/10.5194/acp-18-8757->
907 2018, 2018.
- 908
- 909 Gkikas, A., Giannaros, T.M., Kotroni, V., Lagouvardos, K.: Assessing the radiative impacts of an
910 extreme desert dust outbreak and the potential improvements on short-term weather forecasts: The
911 case of February 2015, *Atmos. Res.*, 226, 152–170, <https://doi.org/10.1016/j.atmosres.2019.04.020>,
912 2019.
- 913
- 914 Gkikas, A., Proestakis, E., Amiridis, V., Kazadzis, S., Di Tomaso, E., Tsekeri, A., Marinou, E.,
915 Hatzianastassiou, N., and Pérez García-Pando, C.: ModIs Dust AeroSol (MIDAS): a global fine-
916 resolution dust optical depth data set, *Atmos. Meas. Tech.*, 14, 309–334, <https://doi.org/10.5194/amt->
917 14-309-2021, 2021.
- 918
- 919 Gliß, J., Mortier, A., Schulz, M., Andrews, E., Balkanski, Y., Bauer, S. E., Benedictow, A. M. K.,
920 Bian, H., Checa-Garcia, R., Chin, M., Ginoux, P., Griesfeller, J. J., Heckel, A., Kipling, Z., Kirkevåg,
921 A., Kokkola, H., Laj, P., Le Sager, P., Lund, M. T., Lund Myhre, C., Matsui, H., Myhre, G., Neubauer,
922 D., van Noije, T., North, P., Olivié, D. J. L., Rémy, S., Sogacheva, L., Takemura, T., Tsigaridis, K.,
923 and Tsyro, S. G.: AeroCom phase III multi-model evaluation of the aerosol life cycle and optical
924 properties using ground- and space-based remote sensing as well as surface in situ observations,
925 *Atmos. Chem. Phys.*, 21, 87–128, <https://doi.org/10.5194/acp-21-87-2021>, 2021.
- 926
- 927 Hamidi, M., Kavianpour, M. R., and Shao, Y.: Synoptic analysis of dust storms in the Middle East,
928 *Asia-Pac. J. Atmos. Sci.*, 49, 279–286, 2013.
- 929
- 930 Hand, J. L., Gill, T. E., and Schichtel, B. A.: Spatial and seasonal variability in fine mineral dust and
931 coarse aerosol mass at re-mote sites across the United States, *J. Geophys. Res.-Atmos.*, 122, 3080–
932 3097, <https://doi.org/10.1002/2016jd026290>, 2017.
- 933
- 934 Haywood, J. and Boucher, O.: Estimates of the direct and indirect radiative forcing due to
935 tropospheric aerosols: A review, *Rev. Geophys.*, 38, 513–543,
936 <https://doi.org/10.1029/1999RG000078>, 2000.
- 937
- 938 Huang, J., Lin, B., Minnis, P., Wang, T., Wang, X., Hu, Y., Yi, Y., and Ayers, J. K.: Satellite-based
939 assessment of possible dust aerosols semi-direct effect on cloud water path over East Asia, *Geophys.*
940 *Res. Lett.*, 33, L19802, <https://doi.org/10.1029/2006GL026561>, 2006.



941
942 Huneus, N., Schulz, M., Balkanski, Y., Griesfeller, J., Prospero, J., Kinne, S., Bauer, S., Boucher,
943 O., Chin, M., Dentener, F., Diehl, T., Easter, R., Fillmore, D., Ghan, S., Ginoux, P., Grini, A.,
944 Horowitz, L., Koch, D., Krol, M. C., Landing, W., Liu, X., Mahowald, N., Miller, R., Morcrette, J.-
945 J., Myhre, G., Penner, J., Perlwitz, J., Stier, P., Takemura, T., and Zender, C. S.: Global dust model
946 intercomparison in AeroCom phase I, *Atmos. Chem. Phys.*, 11, 7781-7816,
947 <https://doi.org/10.5194/acp-11-7781-2011>, 2011.

948
949 Husar, R. B., Tratt, D. M., Schichtel, D. M., Falke, S. R., Li, F., Jaffe, D., Gassó, S., Gill, T.,
950 Laulainen, N. S., Lu, F., Reheis, M. C., Chun, Y., Westphal, D., Holben, B. N., Gueymard, C., McK-
951 endry, I., Kuring, N., Feldman, G. C., McClain, C., Frouin, R. J., Merrill, J., DuBois, D., Vignola, F.,
952 Murayama, T., Nickovic, S., Wilson, W. E., Sassen, K., Sugimoto, N., and Malm, W. C.: Asian dust
953 events of April 1998, *J. Geophys. Res.*, 106, 18317–18330, <https://doi.org/10.1029/2000JD900788>,
954 2001.

955
956 Ignatov, A. and Stowe, L.: Physical Basis, Premises, and SelfConsistency Checks of Aerosol
957 Retrievals from TRMM VIRS, *J. Appl. Meteor.*, 39, 2259–2277, <https://doi.org/10.1175/1520->
958 [0450\(2001\)040<2259:PBPASC>2.0.CO;2](https://doi.org/10.1175/1520-0450(2001)040<2259:PBPASC>2.0.CO;2), 2000.

959
960 Indoitu, R., Kozhoridze, G., Batyrbaeva, M., Vitkovskaya, I., Orlovsky, N., Blumberg, D., Orlovsky,
961 L.: Dust emission and environmental changes in the dried bottom of the Aral Sea. *Aeolian. Res.* 17,
962 101–115, 2015, <https://doi.org/10.1016/j.aeolia.2015.02.004>.

963
964 Jickells, T. D., An, Z. S., Andersen, K. K., Baker, A. R., Bergametti, G., Brooks, N., Cao, J. J., Boyd,
965 P. W., Duce, R. A., Hunter, K. A., Kawahata, H., Kubilay, N., laRoche, J., Liss, P. S., Mahowald, N.,
966 Prospero, J. M., Ridgwell, A. J., Tegen, I., and Torres, R.: Global iron connections between desert
967 dust, ocean biogeochemistry, and climate, *Science*, 308, 67–71, 2005.

968
969 Jickells, T., Boyd, P., and Hunter, K.: Biogeochemical impacts of dust on the global carbon cycle, in:
970 *Mineral Dust*, edited by: Knippertz, P. and Stuut, J.-B. W., Springer, the Netherlands, 359–384, 2014.

971
972 Jin, Q., Wei, J., Pu, B., Yang, Z.-L., and Parajuli, S. P.: High summertime aerosol loadings over the
973 Arabian Sea and their transport pathways. *Journal of Geophysical Research: Atmospheres*, 123, 10,568–10,590, <https://doi.org/10.1029/2018JD028588>, 2018.

974
975



- 976 Johnson, M. S., Meskhidze, N., Kiliyanpilakkil, V. P., and Gassó, S.: Understanding the transport of
977 Patagonian dust and its influence on marine biological activity in the South Atlantic Ocean, *Atmos.*
978 *Chem. Phys.*, 11, 2487–2502, <https://doi.org/10.5194/acp-11-2487-2011>, 2011.
979
- 980 Kanakidou, M., Mihalopoulos, N., Kindap, T., Im, U., Vrekoussis, M., Gerasopoulos, E., Dermizaki,
981 E., Unal, A., Kocak, M., Markakis, K., Melas, D., Kouvarakis, G., Youssef, A. F., Richter, A.,
982 Hatzianastassiou, N., Hilboll, A., Ebojje, F., Wittrock, F., von Savigny, C., Burrows, J. P.,
983 Ladstaetter-Weissenmayer, A., and Moubasher, H.: Megacities as hot spots of air pollution in the
984 East Mediterranean, *Atmos. Environ.*, 45, 1223–1235,
985 <https://doi.org/10.1016/j.atmosenv.2010.11.048>, 2011.
986
- 987 Kanatani, K.T., Ito, I., Al-Delaimy, W.K., Adachi, Y., Mathews, W.C., Ramsdell, J.W.: Toyama
988 Asian Desert Dust and Asthma Study Group Members. Desert dust exposure is associated with
989 increased risk of asthma hospitalization in children, *Am. J. Respir. Crit. Care Med.* 182 (12),
990 1475e1481. <https://doi.org/10.1164/rccm.201002-0296OC>, 2010.
991
- 992 Kinne, S., Schulz, M., Textor, C., Guibert, S., Balkanski, Y., Bauer, S. E., Berntsen, T., Berglen, T.
993 F., Boucher, O., Chin, M., Collins, W., Dentener, F., Diehl, T., Easter, R., Feichter, J., Fillmore, D.,
994 Ghan, S., Ginoux, P., Gong, S., Grini, A., Hendricks, J., Herzog, M., Horowitz, L., Isaksen, I., Iversen,
995 T., Kirkevåg, A., Kloster, S., Koch, D., Kristjansson, J. E., Krol, M., Lauer, A., Lamarque, J. F.,
996 Lesins, G., Liu, X., Lohmann, U., Montanaro, V., Myhre, G., Penner, J., Pitari, G., Reddy, S., Seland,
997 O., Stier, P., Takemura, T., and Tie, X.: An AeroCom initial assessment – optical properties in aerosol
998 component modules of global models, *Atmos. Chem. Phys.*, 6, 1815–1834,
999 <https://doi.org/10.5194/acp-6-1815-2006>, 2006.
1000
- 1001 Klose, M., Shao, Y., Karremann, M. K., and Fink, A.: Sahel dust zone and synoptic background,
1002 *Geophys. Res. Lett.*, 37, L09802, <https://doi.org/10.1029/2010GL042816>, 2010.
1003
- 1004 Knight, A. W., McTainsh, G. H., & Simpson, R. W.: Sediment loads in an Australian dust storm—
1005 Implications for present and past dust processes. *Catena*, 24(3), 195–213,
1006 [https://doi.org/10.1016/0341-8162\(95\)00026-O](https://doi.org/10.1016/0341-8162(95)00026-O), 1995.
1007
- 1008 Knippertz, P., Deutscher, C., Kandler, K., Müller, T., Schulz, O., and Schütz, L.: Dust mobilization
1009 due to density currents in the Atlas region: Observations from the Saharan Mineral Dust Experiment



- 1010 2006 field campaign, *J. Geophys. Res.-Atmos.*, 112, 1–14, <https://doi.org/10.1029/2007JD008774>,
1011 2007.
1012
- 1013 Knippertz, P., Evans, M., Field, P. R., Fink, A. H., Liousse, C., and Marsham, J. H.: The possible role
1014 of local air pollution in climate change in West Africa, *Nat. Clim. Chang.*, 5, 815–822,
1015 <https://doi.org/10.1038/NCLIMATE2727>, 2015.
1016
- 1017 Knippertz, P. and Todd, M. C.: Mineral Dust Aerosols over the Sahara: Meteorological Controls on
1018 Emission and Transport and Implications for Modeling, *Rev. Geophys.*, 50, RG1007,
1019 <https://doi.org/10.1029/2011RG000362>, 2012.
1020
- 1021 Koch, J. and Renno, N. O.: The role of convective plumes and vortices on the global aerosol budget,
1022 *Geophys. Res. Lett.*, 32, L18806, doi:10.1029/2005GL023420, 2005.
1023
- 1024 Kok, J. F., Adebisi, A. A., Albani, S., Balkanski, Y., Checa-Garcia, R., Chin, M., Colarco, P. R.,
1025 Hamilton, D. S., Huang, Y., Ito, A., Klose, M., Leung, D. M., Li, L., Mahowald, N. M., Miller, R. L.,
1026 Obiso, V., Pérez García-Pando, C., Rocha-Lima, A., Wan, J. S., and Whicker, C. A.: Improved
1027 representation of the global dust cycle using observational constraints on dust properties and
1028 abundance, *Atmos. Chem. Phys.*, 21, 8127–8167, <https://doi.org/10.5194/acp-21-8127-2021>, 2021a.
1029
- 1030 Kok, J. F., Adebisi, A. A., Albani, S., Balkanski, Y., Checa-Garcia, R., Chin, M., Colarco, P. R.,
1031 Hamilton, D. S., Huang, Y., Ito, A., Klose, M., Li, L., Mahowald, N. M., Miller, R. L., Obiso, V.,
1032 Pérez García-Pando, C., Rocha-Lima, A., and Wan, J. S.: Contribution of the world's main dust source
1033 regions to the global cycle of desert dust, *Atmos. Chem. Phys.*, 21, 8169–8193,
1034 <https://doi.org/10.5194/acp-21-8169-2021>, 2021b.
1035
- 1036 Koren, I., Yoram, J. K., Richard, W., Martin, C. T., Yinon, R., Martins, J. V., and Daniel, R.: The
1037 Bodélé depression: a single spot in the Sahara that provides most of the mineral dust to the Amazon
1038 forest, *Environ. Res. Lett.*, 1, 014005, <https://doi.org/10.1088/1748-9326/1/1/014005>, 2006.
1039
- 1040 Kosmopoulos, P.G., Kazadzis, S., El-Askary, H., Taylor, M., Gkikas, A., Proestakis, E., Kontoes, C.,
1041 El-Khayat, M.M.: Earth-Observation-Based Estimation and Forecasting of Particulate Matter Impact
1042 on Solar Energy in Egypt, *Remote Sens.*, 10, 1870, 2018.
1043



- 1044 Lambert, F., Kug, J.-S., Park, R. J., Mahowald, N., Winckler, G., Abe-Ouchi, A., O'ishi, R.,
1045 Takemura, T., and Lee, J.-H.: The role of mineral-dust aerosols in polar temperature amplification,
1046 Nat. Clim. Change, 3, 487–491, <https://doi.org/10.1038/nclimate1785>, 2013.
1047
- 1048 Levy, R. C., Leptoukh, G. G., Kahn, R., Zubko, V., Gopalan, A., and Remer, L. A.: A critical look at
1049 deriving monthly aerosol optical depth from satellite data, IEEE T. Geosci. Remote, 47, 2942–2956,
1050 <https://doi.org/10.1109/TGRS.2009.2013842>, 2009.
1051
- 1052 Levy, R. C., Mattoo, S., Munchak, L. A., Remer, L. A., Sayer, A. M., Patadia, F., and Hsu, N. C.:
1053 The Collection 6 MODIS aerosol products over land and ocean, Atmos. Meas. Tech., 6, 2989–3034,
1054 <https://doi.org/10.5194/amt-6-2989-2013>, 2013.
1055
- 1056 Li, L., and Sokolik, I.: Analysis of Dust Aerosol Retrievals Using Satellite Data in Central Asia,
1057 Atmosphere, 9, 288, 2018.
1058
- 1059 Liu, D., Wang, Z., Liu, Z., Winker, D., and Trepte, C.: A height resolved global view of dust aerosols
1060 from the first year CALIPSO lidar measurements, J. Geophys. Res.-Atmos., 113, D16214,
1061 <https://doi.org/10.1029/2007JD009776>, 2008.
1062
- 1063 Mahowald, N. M. and Luo, C.: A less dusty future?, Geophys. Res.Lett., 30, 1903,
1064 <https://doi.org/10.1029/2003GL017880>, 2003.
1065
- 1066 Marinou, E., Amiridis, V., Biniotoglou, I., Tsikerdekis, A., Solomos, S., Proestakis, E., Konsta, D.,
1067 Papagiannopoulos, N., Tsekeri, A., Vlastou, G., Zanis, P., Balis, D., Wandinger, U., and Ansmann,
1068 A.: Three-dimensional evolution of Saharan dust transport towards Europe based on a 9-year
1069 EARLINET-optimized CALIPSO dataset, Atmos. Chem. Phys., 17, 5893–5919,
1070 <https://doi.org/10.5194/acp-17-5893-2017>, 2017.
1071
- 1072 Marticoréna, B.: Mineral Dust - A key player in the Earth system, chap. Chapter 5: Dust production
1073 mechanisms, pp. 93–120, Springer, 2014.
1074
- 1075 Mazzonia, E., & Vazquez, M.: Desertification in Patagonia. In E. M. Latrubesse (Ed.), Natural
1076 hazards and human-exacerbated disasters in Latin America, (Vol. 13, pp. 351–377). Elsevier,
1077 [https://doi.org/https://doi.org/10.1016/S0928-2025\(08\)10017-7](https://doi.org/https://doi.org/10.1016/S0928-2025(08)10017-7), 2009.
1078



- 1079 McConnell, J. R., Aristarain, A. J., Banta, J. R., Edwards, P. R., and Simões, J. C.: 20th-century
1080 doubling in dust archived in an Antarctic Peninsula ice core parallels climate change and
1081 desertification in South America, *Proc. Natl. Acad. Sci. U. S. A.*, 104, 5743–5748, 2007.
1082
- 1083 Micklin, P.: The Aral Sea disaster, *Annu. Rev. Earth Planet. Sci.*, 35, 47–72, 2007.
1084
- 1085 Middleton, N. J.: Dust storms in the Middle East, *J. Arid Environ.*, 10, 83–96, 1986.
1086
- 1087 Middleton, H. J.: Desert dust hazards: A global review, *Aeolian Res.*, 24, 53–63, 2017.
1088
- 1089 Middleton, N. J. and Goudie, A. S.: Saharan dust: sources and trajectories, *T. I. Brit. Geogr.*, 26, 165–
1090 181, doi:10.1111/1475- 5661.00013, 2001.
1091
- 1092 Middleton, N.J., Kang, U.: Sand and dust storms: impact mitigation, *Sustainability*, 9, 1053,
1093 <https://doi.org/10.3390/su9061053>, 2017.
- 1094 Mitchell, R. M., Forgan, B. W., and Campbell, S. K.: The Climatology of Australian Aerosol, *Atmos.*
1095 *Chem. Phys.*, 17, 5131-5154, <https://doi.org/10.5194/acp-17-5131-2017>, 2017.
- 1096 Moran-Zuloaga, D., Ditas, F., Walter, D., Saturno, J., Brito, J., Carbone, S., Chi, X., Hrabě de
1097 Angelis, I., Baars, H., Godoi, R. H. M., Heese, B., Holanda, B. A., Lavrič, J. V., Martin, S. T., Ming,
1098 J., Pöhlker, M. L., Ruckteschler, N., Su, H., Wang, Y., Wang, Q., Wang, Z., Weber, B., Wolff, S.,
1099 Artaxo, P., Pöschl, U., Andreae, M. O., and Pöhlker, C.: Long-term study on coarse mode aerosols in
1100 the Amazon rain forest with the frequent intrusion of Saharan dust plumes, *Atmos. Chem. Phys.*, 18,
1101 10055-10088, <https://doi.org/10.5194/acp-18-10055-2018>, 2018.
1102
- 1103 Nabat, P., Somot, S., Mallet, M., Michou, M., Sevault, F., Driouech, F., Meloni, D., di Sarra, A., Di
1104 Biagio, C., Formenti, P., Sicard, M., Léon, J.-F., and Bouin, M.-N.: Dust aerosol radiative effects
1105 during summer 2012 simulated with a coupled regional aerosol–atmosphere–ocean model over the
1106 Mediterranean, *Atmos. Chem. Phys.*, 15, 3303-3326, <https://doi.org/10.5194/acp-15-3303-2015>,
1107 2015.
1108
- 1109 Okin, G. S., Mahowald, N., Chadwick, O. A., and Artaxo, P.: Impact of desert dust on the
1110 biogeochemistry of phosphorus in terrestrial ecosystems, *Global Biogeochem. Cy.*, 18, GB2005,
1111 <https://doi.org/10.1029/2003GB002145>, 2004.
1112



- 1113 O'Neill, N. T., Ignatov, A., Holben, B. N., and Eck, T. F.: The lognormal distribution as a reference
1114 for reporting aerosol optical depth statistics; Empirical tests using multi-year, multi-site AERONET
1115 Sunphotometer data, *Geophys. Res. Lett.*, 27, 3333–3336, <https://doi.org/10.1029/2000GL011581>,
1116 2000.
1117
- 1118 Pease, P. P., Tchakerian, V. P., and Tindale, N. W.: Aerosols over the Arabian Sea: geochemistry and
1119 source areas for Aeolian desert dust, *J. Arid Environ.*, 39, 477–496,
1120 <https://doi.org/10.1006/jare.1997.0368>, 1998.
1121
- 1122 Pérez, C., Nickovic, S., Pejanovic, G., Baldasano, J. M., and Özsoy, E.: Interactive dust-radiation
1123 modeling: A step to improve weather forecasts, *J. Geophys. Res.*, 111, 1–17, 2006.
1124
- 1125 Pérez García-Pando, C., Stanton, M. C., Diggle, P. J., Trzaska, S., Miller, R. L., Perlwitz, J. P.,
1126 Baldasano, J. M., Cuevas, E., Ceccato, P., Yaka, P., and Thomson, M. C.: Soil Dust Aerosols and
1127 Wind as Predictors of Seasonal Meningitis Incidence in Niger, *Environ. Health Perspect.*, 122, 679–
1128 686, doi:10.1289/ehp.1306640, 2014a.
1129
- 1130 Pérez García-Pando, C., Thomson, M.C., Stanton, M., Diggle, P., Hopson, T., Pandya, R. and Miller,
1131 R.L.: Meningitis and climate: From science to practice. *Earth Perspect.*, 1, 14, doi:10.1186/2194-
1132 6434-1-14, 2014b.
1133
- 1134 Peyridieu, S., Chédin, A., Capelle, V., Tsamalis, C., Pierangelo, C., Armante, R., Crevoisier, C.,
1135 Crépeau, L., Siméon, M., Ducos, F., and Scott, N. A.: Characterisation of dust aerosols in the infrared
1136 from IASI and comparison with PARASOL, MODIS, MISR, CALIOP, and AERONET observations,
1137 *Atmos. Chem. Phys.*, 13, 6065–6082, <https://doi.org/10.5194/acp-13-6065-2013>, 2013.
1138
- 1139 Piketh, S., Annegarn, H., and Tyson, P.: Lower tropospheric aerosol loadings over South Africa: the
1140 relative contribution of aeolian dust, industrial emissions, and biomass burning, *J. Geophys. Res.*, 104,
1141 1597–1607, 1999.
1142
- 1143 Prasad, A. K., Singh, S., Chauhan, S., Srivastava, M. K., Singh, R. P., and Singh, R.: Aerosol radiative
1144 forcing over the IndoGangetic plains during major dust storms, *Atmos. Environ.*, 41, 6289–6301,
1145 doi:10.1016/j.atmosenv.2007.03.060, 2007a.
1146



- 1147 Prasad, A. K. and Singh, R. P.: Changes in aerosol parameters during major dust storm events (2001–
1148 2005) over the Indo-Gangetic Plains using AERONET and MODIS data, *J. Geophys. Res.- Atmos.*,
1149 112, D09208, <https://doi.org/10.1029/2006JD007778>, 2007b.
1150
- 1151 Proestakis, E., Amiridis, V., Marinou, E., Georgoulas, A. K., Solomos, S., Kazadzis, S., Chimot, J.,
1152 Che, H., Alexandri, G., Biniotoglou, I., Daskalopoulou, V., Kourtidis, K. A., de Leeuw, G., and van
1153 der A, R. J.: Nine-year spatial and temporal evolution of desert dust aerosols over South and East
1154 Asia as revealed by CALIOP, *Atmos. Chem. Phys.*, 18, 1337–1362, [https://doi.org/10.5194/acp-18-](https://doi.org/10.5194/acp-18-1337-2018)
1155 1337-2018, 2018.
1156
- 1157 Prospero, J. M.: Long-range transport of mineral dust in the global atmosphere: Impact of African
1158 dust on the environment of the southeastern United States, *P. Natl. Acad. Sci. USA*, 96, 3396–3403,
1159 1999.
1160
- 1161 Prospero, J. M., Collard, F. X., Molinie, J., and Jeannot, A.: Characterizing the annual cycle of
1162 African dust transport to the Caribbean Basin and South America and its impact on the environment
1163 and air quality, *Global Biogeochem. Cy.*, 28, 757–773, <https://doi.org/10.1002/2013gb004802>, 2014.
1164
- 1165 Prospero, J. M., Ginoux, P., Torres, O., Nicholson, S. E., and Gill, T. E.: Environmental
1166 characterization of global sources of atmospheric soil dust identified with the Nimbus 7 Total Ozone
1167 Mapping Spectrometer (TOMS) absorbing aerosol product, *Rev. Geophys.*, 40, 2–1–2–31, 2002.
1168
- 1169 Prospero, J. M. and Lamb, P. J.: African droughts and dust transport to the Caribbean: climate change
1170 implications, *Science*, 302, 1024–1027, doi:10.1126/science.1089915, 2003.
1171
- 1172 Querol X., Tobías, A., Pérez, N., Karanasiou, A., Amato, F., Stafoggia, M., Pérez García-Pando, C.,
1173 Ginoux, P., Forastiere, F., Gumy, S., Mudu, P., Alastuey, A.: Monitoring the impact of desert dust
1174 outbreaks for air quality for health studies, *Environ Int.*, 130:104867, doi:
1175 10.1016/j.envint.2019.05.061. Epub 2019 Jun 14. PMID: 31207476; PMCID: PMC6686079, 2019.
1176
- 1177 Ramaswamy, V.P., Muraleedharan, M., Prakash Babu, C.: Mid-troposphere transport of Middle-East
1178 dust over the Arabian Sea and its effect on rainwater composition and sensitive ecosystems over India.
1179 *Scientific Reports* 7, 13676, <https://doi.org/10.1038/s41598-017-13652-1>, 2017.
1180



- 1181 Rajot, J. L., Formenti, P., Alfaro, S., Desboeufs, K., Chevaillier, S., Chatenet, B., Gaudichet, A.,
1182 Journet, E., Marticorena, B., Triquet, S., Maman, A., Mouget, N., and Zakou, A.: AMMA dust
1183 experiment: An overview of measurements performed during the dry season special observation
1184 period (SOP0) at the Banizoumbou (Niger) supersite, *J. Geophys. Res.*, 113, D00C14,
1185 doi:10.1029/2008jd009906, 2008.
- 1186 Rashki, A., Kaskaoutis, D.G., Francois, P., Kosmopoulos, P.G., Legrand, M.: Dust-storm dynamics
1187 over Sistan region, Iran: seasonality, transport characteristics and affected areas, *Aeol. Res.*, 16, 35–
1188 48, 2015.
- 1189 Ridley, D. A., Heald, C. L., Kok, J. F., and Zhao, C.: An observationally constrained estimate of
1190 global dust aerosol optical depth, *Atmos. Chem. Phys.*, 16, 15097–15117,
1191 <https://doi.org/10.5194/acp-16-15097-2016>, 2016.
1192
- 1193 Rivera Rivera, N. I., Gill, T. E., Gebhart, K. A., Hand, J. L., Bleiweiss, M. P., and Fitzgerald, R. M.:
1194 Wind modeling of Chihuahuan Desert dust outbreaks, *Atmos. Environ.*, 43(2), 347–354,
1195 doi:10.1016/j.atmosenv.2008.09.069, 2009.
1196
- 1197 Rodríguez, S., Cuevas, E., Prospero, J. M., Alastuey, A., Querol, X., López-Solano, J., García, M. I.,
1198 and Alonso-Pérez, S.: Modulation of Saharan dust export by the North African dipole, *Atmos. Chem.*
1199 *Phys.*, 15, 7471–7486, <https://doi.org/10.5194/acp-15-7471-2015>, 2015.
1200
- 1201 Rohrmann, A., Heermance, R., Kapp, P., and Cai, F. L.: Wind as the primary driver of erosion in the
1202 Qaidam Basin, China. *Earth Planet. Sci. Lett.*, 374, 1–10, <https://doi.org/10.1016/j.epsl.2013.03.011>,
1203 2013.
1204
- 1205 Saiko, T.A., Zonn, I.S.: Irrigation expansion and dynamics of desertification in the circum-aral region
1206 of central Asia, *Appl. Geogr.*, 20, 349–367, 2000.
1207
- 1208 Sayer, A. M. and Knobelspiesse, K. D.: How should we aggregate data? Methods accounting for the
1209 numerical distributions, with an assessment of aerosol optical depth, *Atmos. Chem. Phys.*, 19, 15023–
1210 15048, <https://doi.org/10.5194/acp-19-15023-2019>, 2019.
1211
- 1212 Schepanski, K., Tegen, I., Laurent, B., Heinold, B., and Macke, A.: A new Saharan dust source
1213 activation frequency map derived from MSG-SEVIRI IR channels, *Geophys. Res. Lett.*, 34, L18803,
1214 <https://doi.org/10.1029/2007GL030168>, 2007.



- 1215
- 1216 Schepanski, K., Tegen, I., Todd, M. C., Heinold, B., Bönisch, G., Laurent, B., and Macke, A.:
1217 Meteorological processes forcing Saharan dust emission inferred from MSG-SEVIRI observations of
1218 subdaily dust source activation and numerical models, *J. Geophys. Res.-Atmos.*, 114, D10201,
1219 <https://doi.org/10.1029/2008JD010325>, 2009.
- 1220
- 1221 Schepanski, K., Heinold, B., and Tegen, I.: Harmattan, Saharan heat low, and West African monsoon
1222 circulation: modulations on the Saharan dust outflow towards the North Atlantic, *Atmos. Chem.*
1223 *Phys.*, 17, 10223-10243, <https://doi.org/10.5194/acp-17-10223-2017>, 2017.
- 1224
- 1225 Shen, H., Abuduwaili, J., Samat, A., Ma, L.: A review on the research of modern aeolian dust in
1226 Central Asia, *Arab J Geosci.*, 9:625, 2016.
- 1227
- 1228 Sogacheva, L., de Leeuw, G., Rodriguez, E., Kolmonen, P., Georgoulas, A. K., Alexandri, G.,
1229 Kourtidis, K., Proestakis, E., Marinou, E., Amiridis, V., Xue, Y., and van der A, R. J.: Spatial and
1230 seasonal variations of aerosols over China from two decades of multi-satellite observations – Part 1:
1231 ATSR (1995–2011) and MODIS C6.1 (2000–2017), *Atmos. Chem. Phys.*, 18, 11389-11407,
1232 <https://doi.org/10.5194/acp-18-11389-2018>, 2018.
- 1233
- 1234 Sokolik, I. N. and Toon, O. B.: Direct radiative forcing by anthropogenic airborne mineral aerosols,
1235 *Nature*, 381, 681–683, <https://doi.org/10.1038/381681a0>, 1996.
- 1236
- 1237 Song, Q., Zhang, Z., Yu, H., Ginoux, P., and Shen, J.: Global Dust Optical Depth Climatology
1238 Derived from CALIOP and MODIS Aerosol Retrievals on Decadal Time Scales: Regional and
1239 Interannual Variability, *Atmos. Chem. Phys. Discuss.* [preprint], <https://doi.org/10.5194/acp-2021-1>,
1240 in review, 2021.
- 1241
- 1242 Srivastava, A. K., Tiwari, S., Devara, P. C. S., Bisht, D. S., Srivastava, M. K., Tripathi, S. N., Goloub,
1243 P., and Holben, B. N.: Pre-monsoon aerosol characteristics over the Indo-Gangetic Basin:
1244 implications to climatic impact, *Ann. Geophys.*, 29, 789-804, [https://doi.org/10.5194/angeo-29-789-](https://doi.org/10.5194/angeo-29-789-2011)
1245 2011, 2011.
- 1246 Stanelle, T., Bey, I., Raddatz, T., Reick, C., and Tegen, I.: Anthro- pogenically induced changes in
1247 twentieth century mineral dust burden and the associated impact on radiative forcing, *J. Geo- phys.*
1248 *Res.-Atmos.*, 119, 13526–13546, 2014.



- 1249 Stefanski, R. and Sivakumar, M. V. K.: Impacts of sand and dust storms on agriculture and potential
1250 agricultural applications of a SDSWS, IOP Conf. Ser.: Earth Environ. Sci., 7, 012016, doi:
1251 10.1088/1755-1307/7/1/012016, 2009.
1252
- 1253 Sun, Y., Chen, H., Tada, R., Weiss, D., Lin, M., Toyoda, S., Yan, Y., and Isozaki, Y.: ESR signal
1254 intensity and crystallinity of quartz from Gobi and sandy deserts in East Asia and implication for
1255 tracing Asian dust provenance, *Geochem. Geophys. Geosy.*, 14, 2615–2627,
1256 <https://doi.org/10.1002/ggge.20162>, 2013.
1257
- 1258 Tanaka, T. Y. and Chiba, M.: A numerical study of the contributions of dust source regions to the
1259 global dust budget, *Global Planet Change*, 52, 88–104,
1260 <https://doi.org/10.1016/j.gloplacha.2006.02.002>, 2006.
- 1261 Tegen, I., Werner, M., Harrison, S., and Kohfeld, K.: Relative im- portance of climate and land use
1262 in determining present and fu- ture global soil dust emission, *Geophys. Res. Lett.*, 31, L05105,
1263 <https://doi.org/10.1029/2003GL019216>, 2004.
- 1264 Tegen, I., Heinold, B., Todd, M., Helmert, J., Washington, R., and Dubovik, O.: Modelling soil dust
1265 aerosol in the Bodélé depression during the BoDEX campaign, *Atmos. Chem. Phys.*, 6, 4345–4359,
1266 <https://doi.org/10.5194/acp-6-4345-2006>, 2006.
1267
- 1268 Tong, D. Q., Wang, J. X. L., Gill, T. E., Lei, H., and Wang, B. Y.: Intensified dust storm activity and
1269 Valley fever infection in the southwestern United States, *Geophys. Res. Lett.*, 44, 4304–4312,
1270 <https://doi.org/10.1002/2017gl073524>, 2017.
1271
- 1272 Tyson, P.D., Garstang, M., Swap, R., Kallberg, P., Edwards, M.: An air transport climatology for
1273 subtropical southern Africa. *Int. J. Climatol.* 16 (3), 265–291, 1996.
1274
- 1275 Vickery, K. J., Eckardt, F. D., and Bryant, R. G.: A sub-basin scale dust plume source frequency
1276 inventory for south-ern Africa, 2005–2008, *Geophys. Res. Lett.*, 40, 5274–5279,
1277 doi:10.1002/grl.50968, 2013.
1278
- 1279 Voss, K. K., and Evan, A. T.: A new satellite-based global climatology of dust aerosol optical depth.
1280 *Journal of Applied Meteorology and Climatology*, doi:10.1175/jamc-d-19-0194.1, 2020.
1281



- 1282 Wagener, T., Guieu, C., Losno, R., Bonnet, S., and Mahowald, N.: Revisiting atmospheric dust export
1283 to the Southern Hemisphere ocean: Biogeochemical implications, *Glob. Biogeochem. Cy.*, 22,
1284 GB2006, <https://doi.org/10.1029/2007gb002984>, 2008.
- 1285
- 1286 Washington, R., Todd, M., Middleton, N. J., and Goudie, A. S.: Dust-storm source areas determined
1287 by the total ozone monitoring spectrometer and surface observations, *Ann. Assoc. Am. Geogr.*, 93,
1288 297–313, <https://doi.org/10.1111/1467-8306.9302003>, 2003.
- 1289
- 1290 Washington, R. and Todd, M. C.: Atmospheric controls on mineral dust emission from the Bodélé
1291 depression, Chad: The role of the low level jet, *Geophys. Res. Lett.*, 32, L17701,
1292 <https://doi.org/10.1029/2005GL023597>, 2005.
- 1293
- 1294 Washington, R., Bouet, C., Cautenet, G., Mackenzie, E., Ashpole, I., Engelstaedter, S., Lizcano, G.,
1295 Henderson, G. M., Schepanski, K., and Tegen, I.: Dust as a tipping element: the Bodélé Depression,
1296 Chad, *P. Natl. Acad. Sci. USA*, 106, 20564–20571, doi:10.1073/pnas.0711850106, 2009.
- 1297
- 1298 Weinzierl, B., Sauer, D., Minikin, A., Reitebuch, O., Dahlkötter, F., Mayer, B., Emde, C., Tegen, I.,
1299 Gasteiger, J., Petzold, A., Veira, A., Kueppers, U., and Schumann, U.: On the visibility of airborne
1300 volcanic ash and mineral dust from the pilot's perspective in flight, *Phys Chem Earth*, 45-46, 87-102,
1301 10.1016/j.pce.2012.04.003, 2012.
- 1302
- 1303 Winker, D. M., Vaughan, M. A., Omar, A., Hu, Y., Powell, K. A., Liu, Z., Hunt, W. H. and Young,
1304 S. A.: Overview of the CALIPSO Mission and CALIOP Data Processing Algorithms, *J. Atmos.*
1305 *Oceanic Technol.*, 26(11), 2310–2323, doi:10.1175/2009JTECHA1281.1, 2009.
- 1306
- 1307 Yu, H. B., Chin, M., Winker, D. M., Omar, A. H., Liu, Z. Y., Kittaka, C., and Diehl, T.: Global view
1308 of aerosol vertical distributions from CALIPSO lidar measurements and GOCART simulations:
1309 Regional and seasonal variations, *J. Geophys. Res.-Atmos.*, 115, D00H30,
1310 <https://doi.org/10.1029/2009jd013364>, 2010.
- 1311
- 1312 Yu, H. B., Chin, M., Yuan, T. L., Bian, H. S., Remer, L. A., Prospero, J. M., Omar, A., Winker, D.,
1313 Yang, Y. K., Zhang, Y., Zhang, Z. B., and Zhao, C.: The fertilizing role of African dust in the Amazon
1314 rainforest: A first multiyear assessment based on data from Cloud-Aerosol Lidar and Infrared
1315 Pathfinder Satellite Observations, *Geophys. Res. Lett.*, 42, 1984–1991,
1316 <https://doi.org/10.1002/2015gl063040>, 2015.



1317

1318 Yu, H., Remer, L. A., Chin, M., Bian, H., Kleidman, R. G., and Diehl, T.: A satellite-based assessment
1319 of transpacific transport of pollution aerosol, *J. Geophys. Res.-Atmos.*, 113, D14S12,
1320 <https://doi.org/10.1029/2007JD009349>, 2008.

1321

1322 Yu, Y., Kalashnikova, O. V., Garay, M. J., and Notaro, M.: Climatology of Asian dust activation and
1323 transport potential based on MISR satellite observations and trajectory analysis, *Atmos. Chem. Phys.*,
1324 19, 363-378, <https://doi.org/10.5194/acp-19-363-2019>, 2019.

1325

1326 Yu, Y., Notaro, M., Kalashnikowa, O., Garay, M.: Climatology of summer Shamal wind in the
1327 Middle East, *J. Geophys. Res.-Atmos.* 121 (1), 289–305, 2016.

1328

1329 Yu, Y., Notaro, M., Liu, Z., Kalashnikova, O., Alkolibi, F., Fadda, E., and Bakhrijy, F.: Assessing
1330 temporal and spatial variations in atmospheric dust over Saudi Arabia through satellite, radiometric,
1331 and station data, *J. Geophys. Res.-Atmos.*, 118, 13253– 13264,
1332 <https://doi.org/10.1002/2013JD020677>, 2013.

1333

1334 Yu, Y., Kalashnikova, O. V., Garay, M. J., Lee, H., Choi, M., Okin, G. S., Yorks, J. E., Campbell, J.
1335 R., and Marquis, J.: A global analysis of diurnal variability in dust and dust mixture using CATS
1336 observations, *Atmos. Chem. Phys.*, 21, 1427–1447, <https://doi.org/10.5194/acp-21-1427-2021>, 2021.

1337

1338 Xi, X. and Sokolik, I. N.: Seasonal dynamics of threshold friction velocity and dust emission in
1339 Central Asia, *J. Geophys. Res. Atmos.*, 120(4), 1536–1564, [doi:10.1002/2014JD022471](https://doi.org/10.1002/2014JD022471), 2015.

1340

1341 Zender, C. S., Huiheng, B., and Newman, D.: Mineral Dust Entrainment and Deposition (DEAD)
1342 model: Description and 1990s dust climatology, *J. Geophys. Res.*, 108, 4416,
1343 <https://doi.org/10.1029/2002JD002775>, 2003.

1344

1345

1346

1347

1348

1349

1350

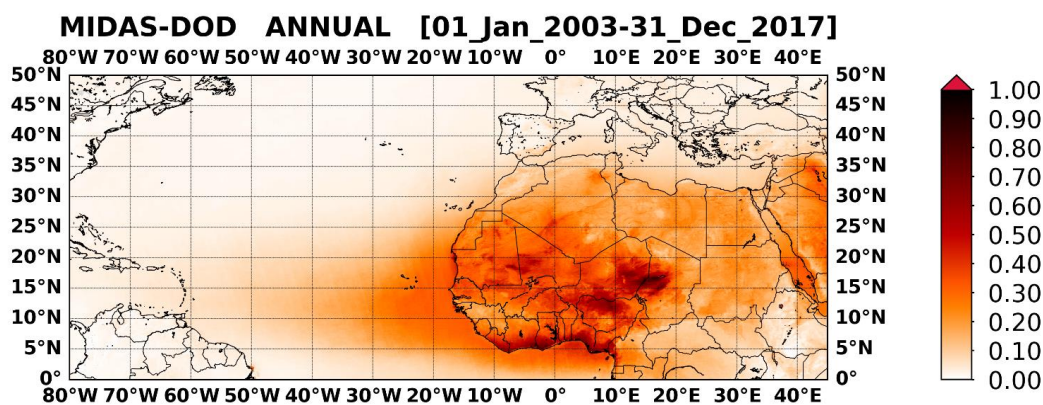
1351



1352 **Table 1:** Annual and seasonal DOD averages, representative for the period 2003-2017, along with the associated
 1353 uncertainty. The first three rows refer to the whole globe (GLB), the global land (GLB-land) and global ocean (GLB-
 1354 ocean). In the fourth and fifth line are given the results for N. Hemisphere (NHE) and S. Hemisphere (SHE) DODs
 1355 whereas in the rest 17 entries the corresponding results for selected subregions (denoted with colored rectangles in Fig. 7
 1356 in Gkikas et al. (2021)) are given.

| REGION | ANNUAL | DJF | MAM | JJA | SON |
|------------------|---------------|---------------|---------------|---------------|---------------|
| GLB | 0.032 ± 0.003 | 0.025 ± 0.004 | 0.043 ± 0.005 | 0.040 ± 0.005 | 0.022 ± 0.004 |
| GLB-land | 0.070 ± 0.005 | 0.063 ± 0.008 | 0.104 ± 0.011 | 0.083 ± 0.010 | 0.049 ± 0.007 |
| GLA-ocean | 0.019 ± 0.002 | 0.015 ± 0.003 | 0.026 ± 0.003 | 0.023 ± 0.003 | 0.012 ± 0.003 |
| NHE | 0.056 ± 0.004 | 0.043 ± 0.005 | 0.085 ± 0.009 | 0.071 ± 0.008 | 0.036 ± 0.005 |
| SHE | 0.008 ± 0.001 | 0.010 ± 0.003 | 0.008 ± 0.002 | 0.006 ± 0.002 | 0.008 ± 0.003 |
| BOD | 0.533 ± 0.009 | 0.483 ± 0.018 | 0.614 ± 0.020 | 0.603 ± 0.017 | 0.451 ± 0.013 |
| GOB | 0.092 ± 0.007 | 0.074 ± 0.010 | 0.189 ± 0.023 | 0.078 ± 0.010 | 0.056 ± 0.005 |
| CAS | 0.126 ± 0.007 | 0.084 ± 0.012 | 0.158 ± 0.016 | 0.144 ± 0.011 | 0.100 ± 0.007 |
| NME | 0.227 ± 0.006 | 0.120 ± 0.009 | 0.319 ± 0.016 | 0.271 ± 0.011 | 0.186 ± 0.009 |
| SUS | 0.018 ± 0.001 | 0.009 ± 0.002 | 0.033 ± 0.005 | 0.021 ± 0.003 | 0.010 ± 0.001 |
| TAK | 0.246 ± 0.020 | 0.114 ± 0.015 | 0.504 ± 0.047 | 0.259 ± 0.030 | 0.130 ± 0.018 |
| THA | 0.198 ± 0.007 | 0.086 ± 0.006 | 0.291 ± 0.013 | 0.424 ± 0.033 | 0.109 ± 0.006 |
| WSA | 0.302 ± 0.006 | 0.199 ± 0.008 | 0.362 ± 0.015 | 0.418 ± 0.016 | 0.237 ± 0.009 |
| EAS | 0.077 ± 0.005 | 0.072 ± 0.014 | 0.130 ± 0.012 | 0.056 ± 0.010 | 0.048 ± 0.006 |
| ENP | 0.020 ± 0.002 | 0.011 ± 0.002 | 0.047 ± 0.005 | 0.017 ± 0.004 | 0.013 ± 0.002 |
| ETA | 0.146 ± 0.007 | 0.109 ± 0.011 | 0.169 ± 0.015 | 0.202 ± 0.015 | 0.093 ± 0.009 |
| GOG | 0.309 ± 0.021 | 0.417 ± 0.032 | 0.416 ± 0.066 | 0.064 ± 0.021 | 0.100 ± 0.022 |
| MED | 0.081 ± 0.003 | 0.052 ± 0.008 | 0.106 ± 0.009 | 0.096 ± 0.006 | 0.066 ± 0.005 |
| SME | 0.250 ± 0.008 | 0.154 ± 0.009 | 0.318 ± 0.016 | 0.394 ± 0.020 | 0.166 ± 0.008 |
| SSA | 0.326 ± 0.013 | 0.309 ± 0.015 | 0.494 ± 0.041 | 0.241 ± 0.054 | 0.199 ± 0.020 |
| WNP | 0.028 ± 0.002 | 0.017 ± 0.003 | 0.064 ± 0.008 | 0.023 ± 0.006 | 0.018 ± 0.002 |
| WTA | 0.035 ± 0.003 | 0.006 ± 0.002 | 0.035 ± 0.005 | 0.090 ± 0.009 | 0.017 ± 0.004 |

1357
 1358
 1359
 1360
 1361
 1362
 1363

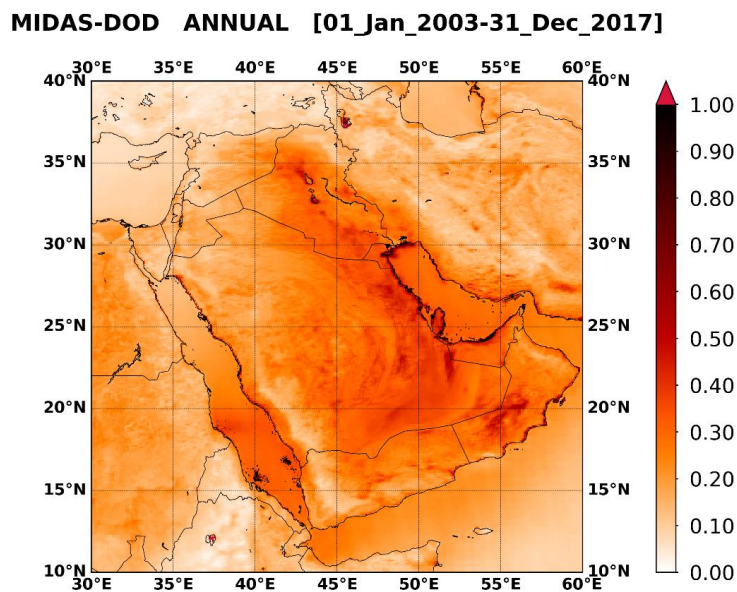


1364

1365 **Figure 1:** Geographical distribution of the MIDAS annual DOD at 550nm, representative for the period 1 January 2003

1366 – 31 December 2017, over North Africa, the Tropical Atlantic Ocean and the broader Mediterranean basin.

1367



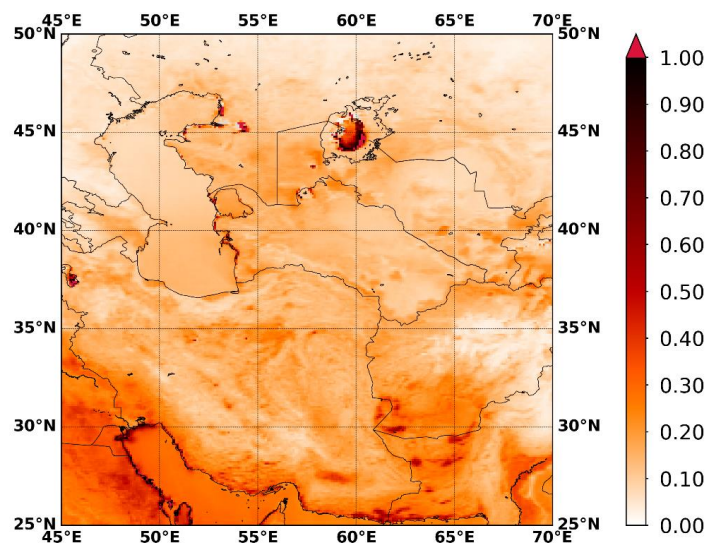
1368

1369 **Figure 2:** As in Figure 1 but for the broader area of the Middle East.

1370



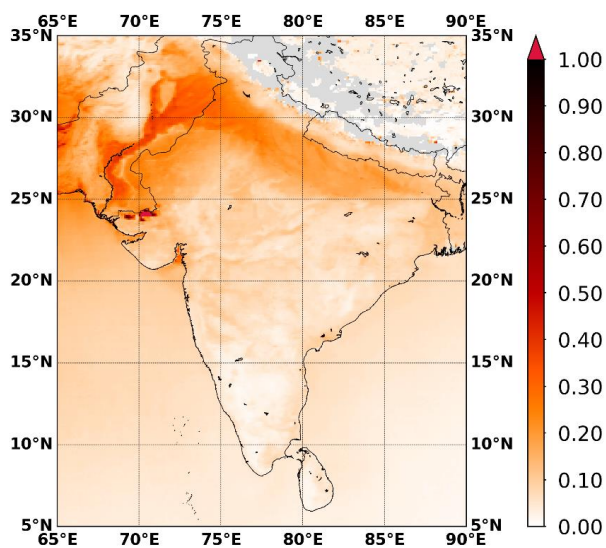
MIDAS-DOD ANNUAL [01_Jan_2003-31_Dec_2017]



1371
1372
1373

Figure 3: As in Figure 1 but for central and southwestern Asia.

MIDAS-DOD ANNUAL [01_Jan_2003-31_Dec_2017]



1374
1375
1376

Figure 4: As in Figure 1 but for the Indian subcontinent.



1377
1378
1379

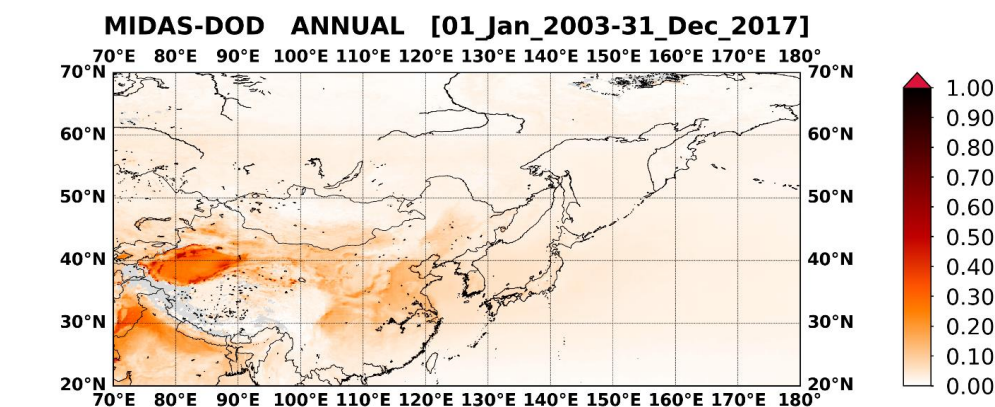


Figure 5: As in Figure 1 but for East Asia and the North Pacific Ocean.

1380
1381
1382

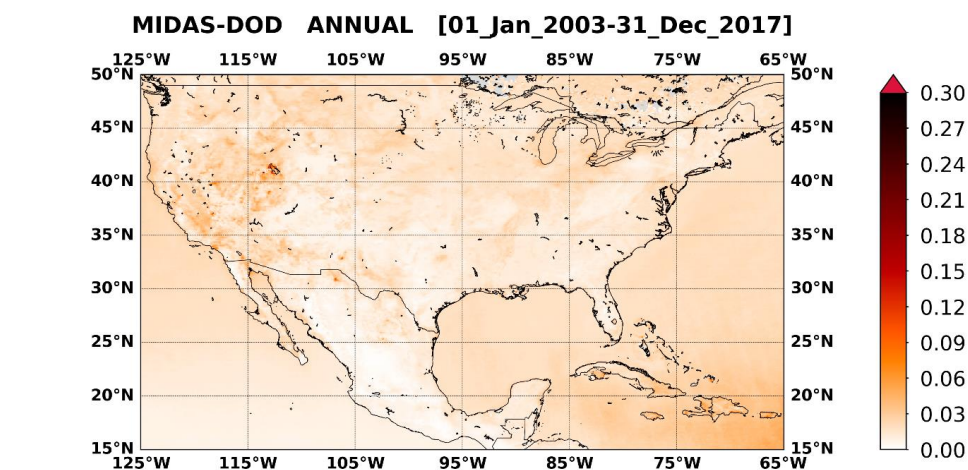


Figure 6: As in Figure 1 but for North America.

1383
1384
1385

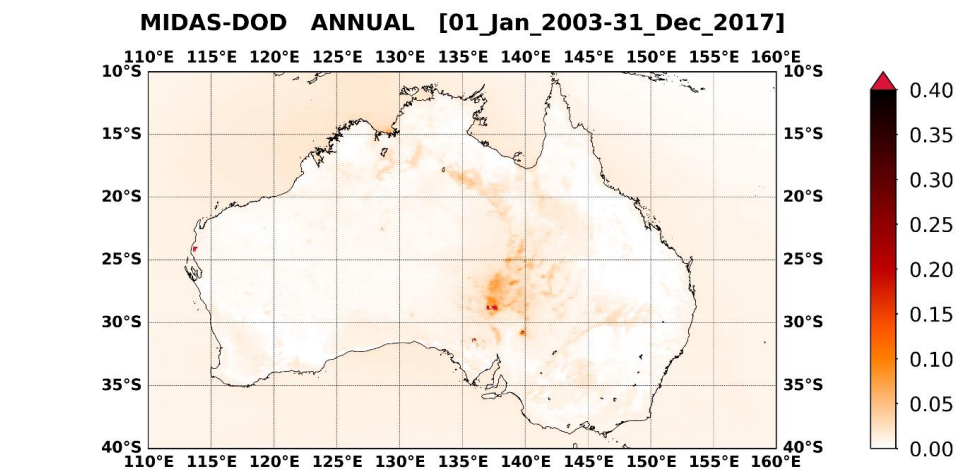
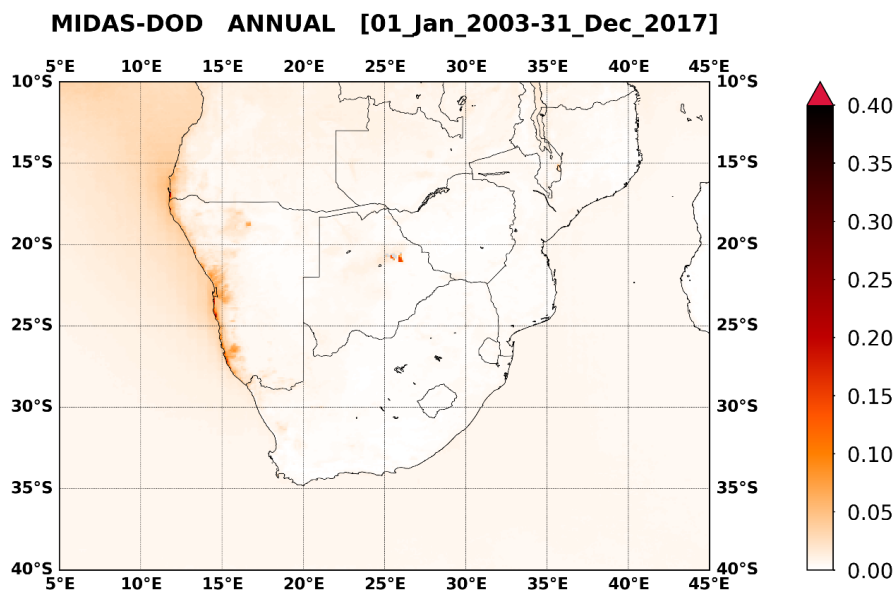


Figure 7: As in Figure 1 but for Australia.

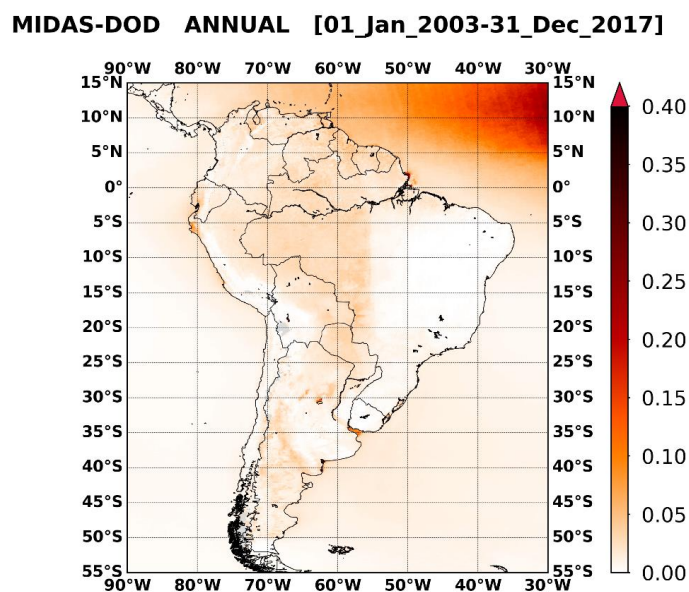


1386



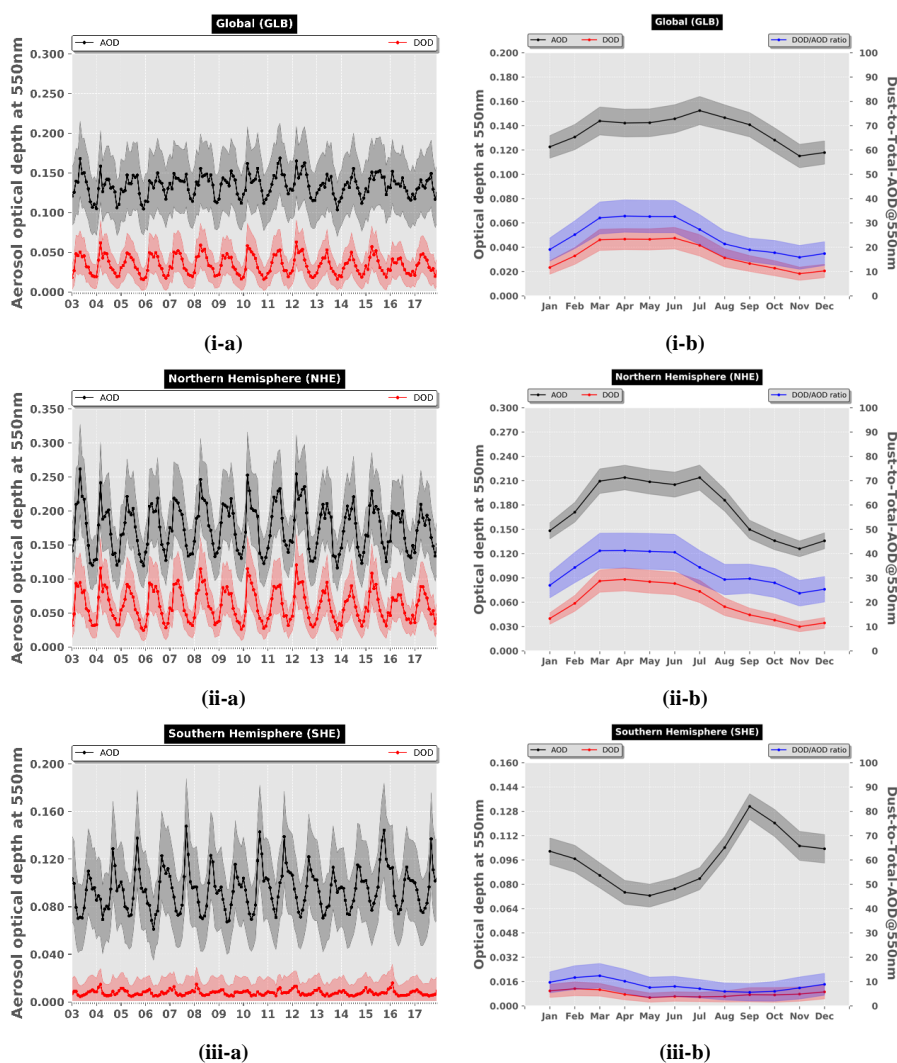
1387
1388
1389

Figure 8: As in Figure 1 but for Southern Africa.



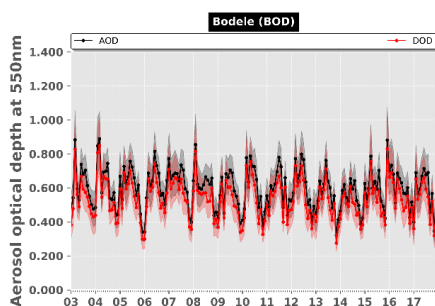
1390
1391
1392
1393
1394
1395
1396
1397
1398
1399
1400

Figure 9: As in Figure 1 but for South America.

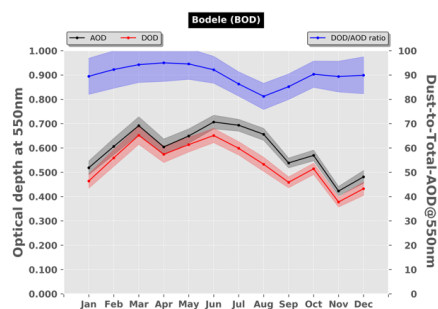


1401 **Figure 10:** Inter-annual (-a) and intra-annual (-b) variability, representative for the period 2007 – 2016, of monthly
 1402 MODIS AOD_{550nm} (black curve) and DOD_{550nm} (red curve) regionally averaged for: (i) the whole globe (GLB), (ii)
 1403 Northern Hemisphere (NHE) and (iii) the Southern Hemisphere (SHE). The blue curves in the intra-annual plots depict
 1404 the dust-to-total AOD_{550nm} ratio (expressed in percentage; right y-axis). The shaded areas correspond to the total
 1405 uncertainty.

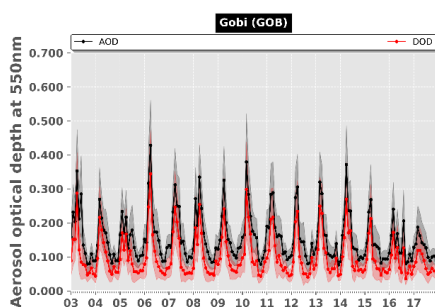
1406
 1407
 1408
 1409
 1410
 1411
 1412
 1413



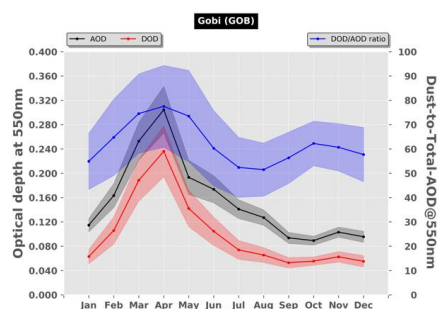
(i-a)



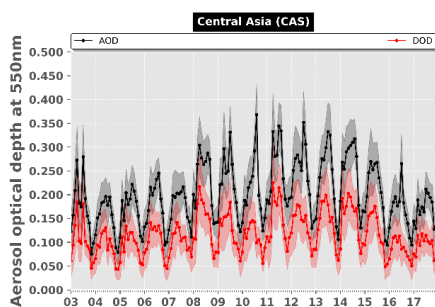
(i-b)



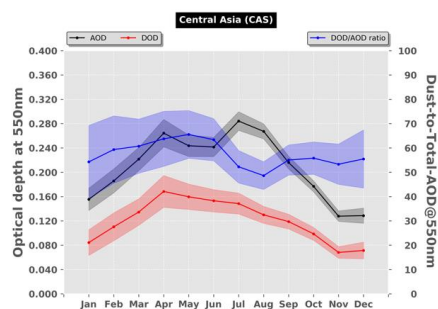
(ii-a)



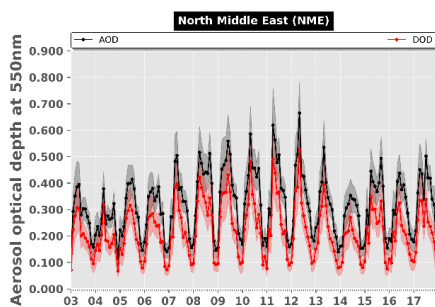
(ii-b)



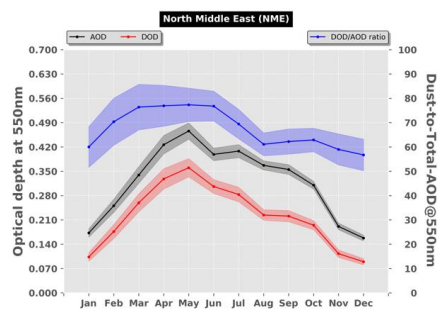
(iii-a)



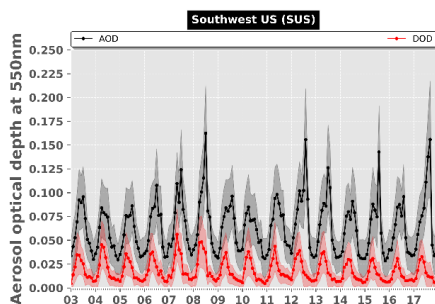
(iii-b)



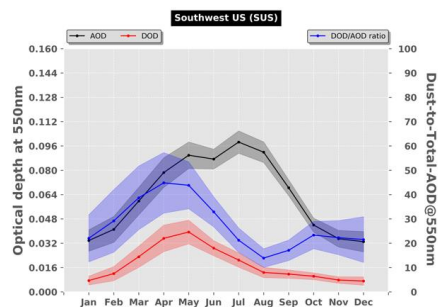
(iv-a)



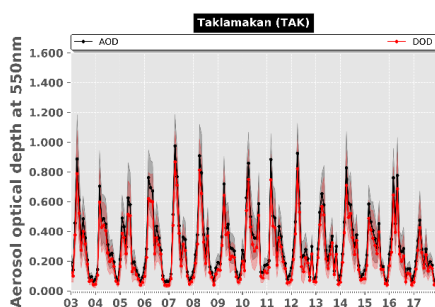
(iv-b)



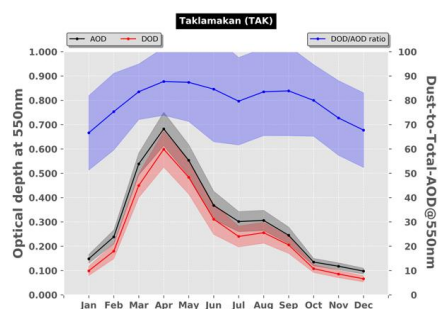
(v-a)



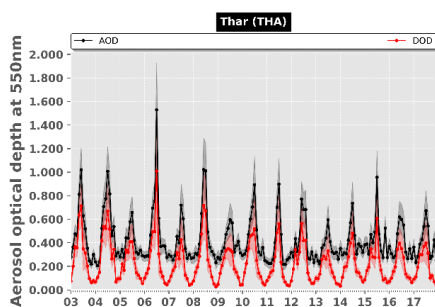
(v-b)



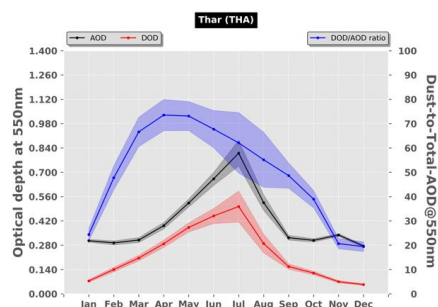
(vi-a)



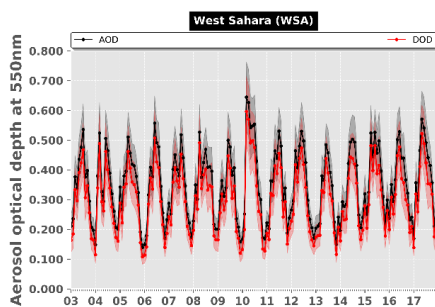
(vi-b)



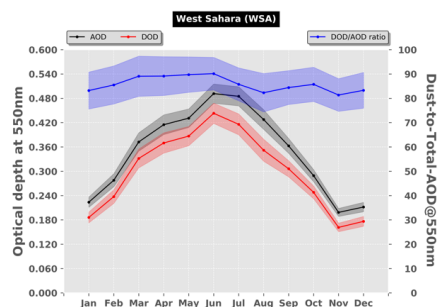
(vii-a)



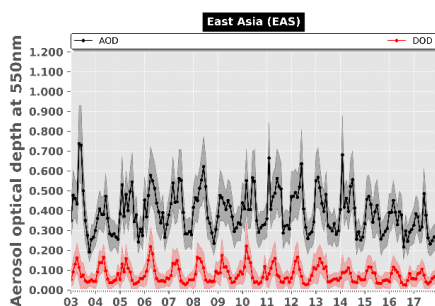
(vii-b)



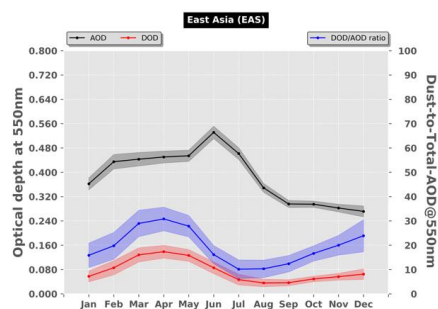
(viii-a)



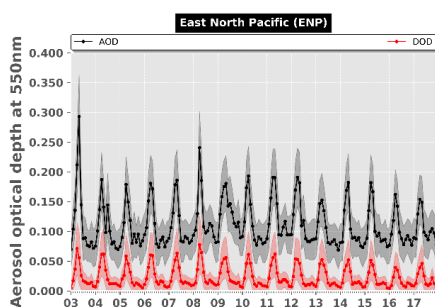
(viii-b)



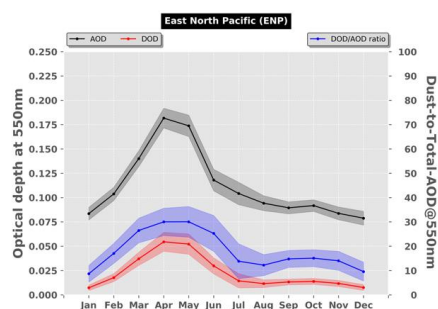
(ix-a)



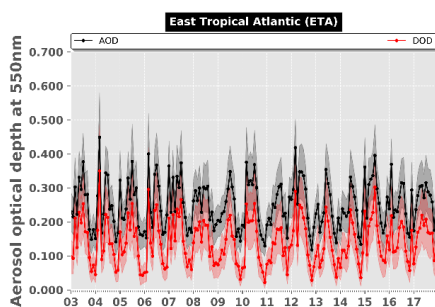
(ix-b)



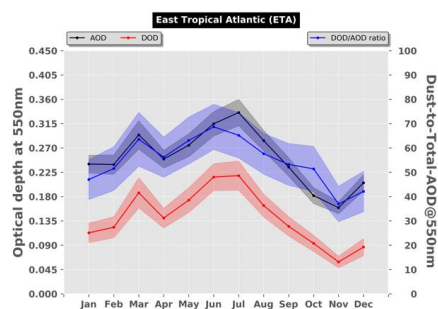
(x-a)



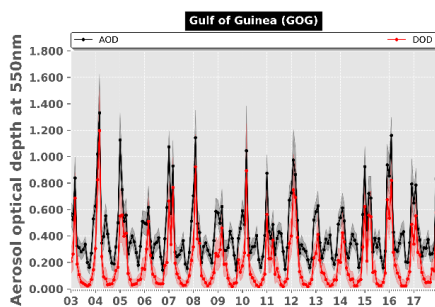
(x-b)



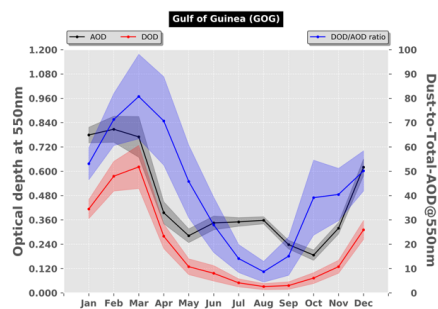
(xi-a)



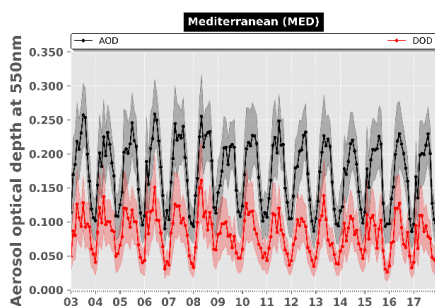
(xi-b)



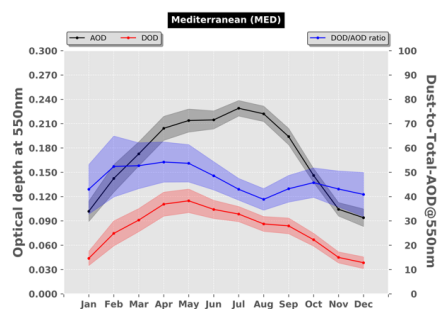
(xii-a)



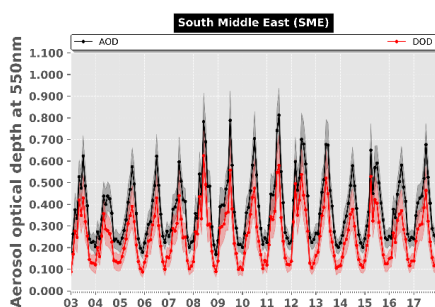
(xii-b)



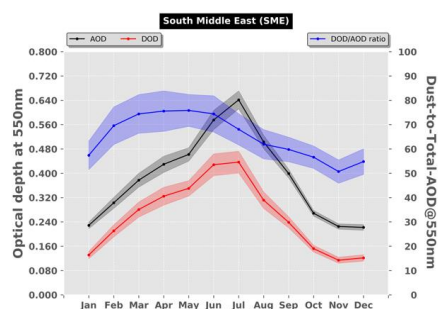
(xiii-a)



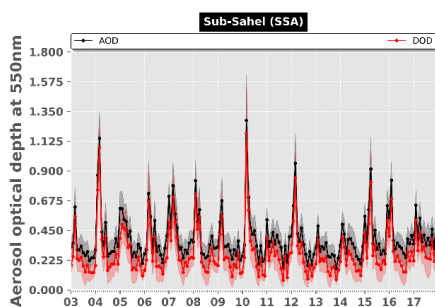
(xiii-b)



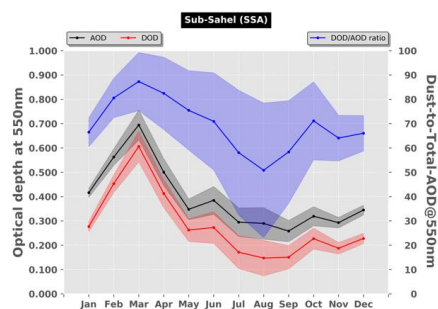
(xiv-a)



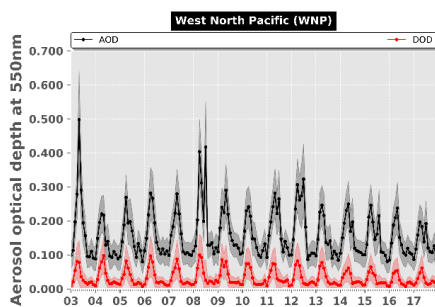
(xiv-b)



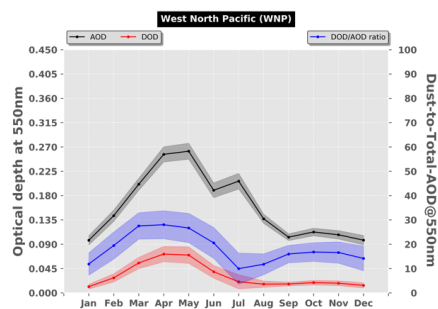
(xv-a)



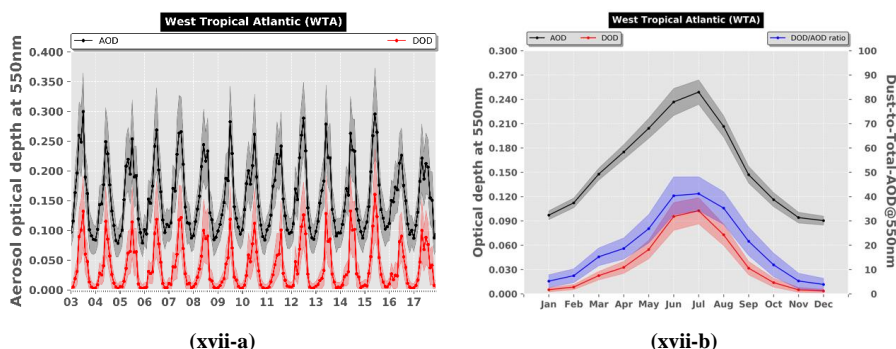
(xv-b)



(xvi-a)



(xvi-b)



1414 **Figure 11:** Inter-annual (-a) and intra-annual (-b) variability, representative for the period 2003 – 2017, of monthly
1415 MODIS AOD_{550nm} (black curve) and DOD_{550nm} (red curve) regionally averaged for: (i) Bodélé Depression (BOD), (ii)
1416 Gobi Desert (GOB), (iii) Central Asia (CAS), (iv) North Middle East (NME), (v) southwest United States (SUS), (vi)
1417 Taklamakan Desert (TAK), (vii) Thar Desert (THA), (viii) West Sahara (WSA), (ix) East Asia (EAS), (x) East North
1418 Pacific (ENP), (xi) East Tropical Atlantic (ETA), (xii) Gulf of Guinea (GOG), (xiii) Mediterranean (MED), (xiv) South
1419 Middle East (SME), (xv) Sub-Sahel (SSA), (xvi) West North Pacific (WNP) and (xvii) West Tropical Atlantic (WTA).
1420 The shaded areas in the inter and intra-annual plots correspond to the total uncertainty. The blue curves in the intra-annual
1421 plots represent the percentage contribution of dust optical depth (DOD) to the aerosol optical depth (AOD).
1422
1423
1424
1425
1426
1427
1428
1429
1430
1431
1432
1433
1434
1435
1436
1437
1438
1439
1440
1441
1442
1443
1444
1445
1446

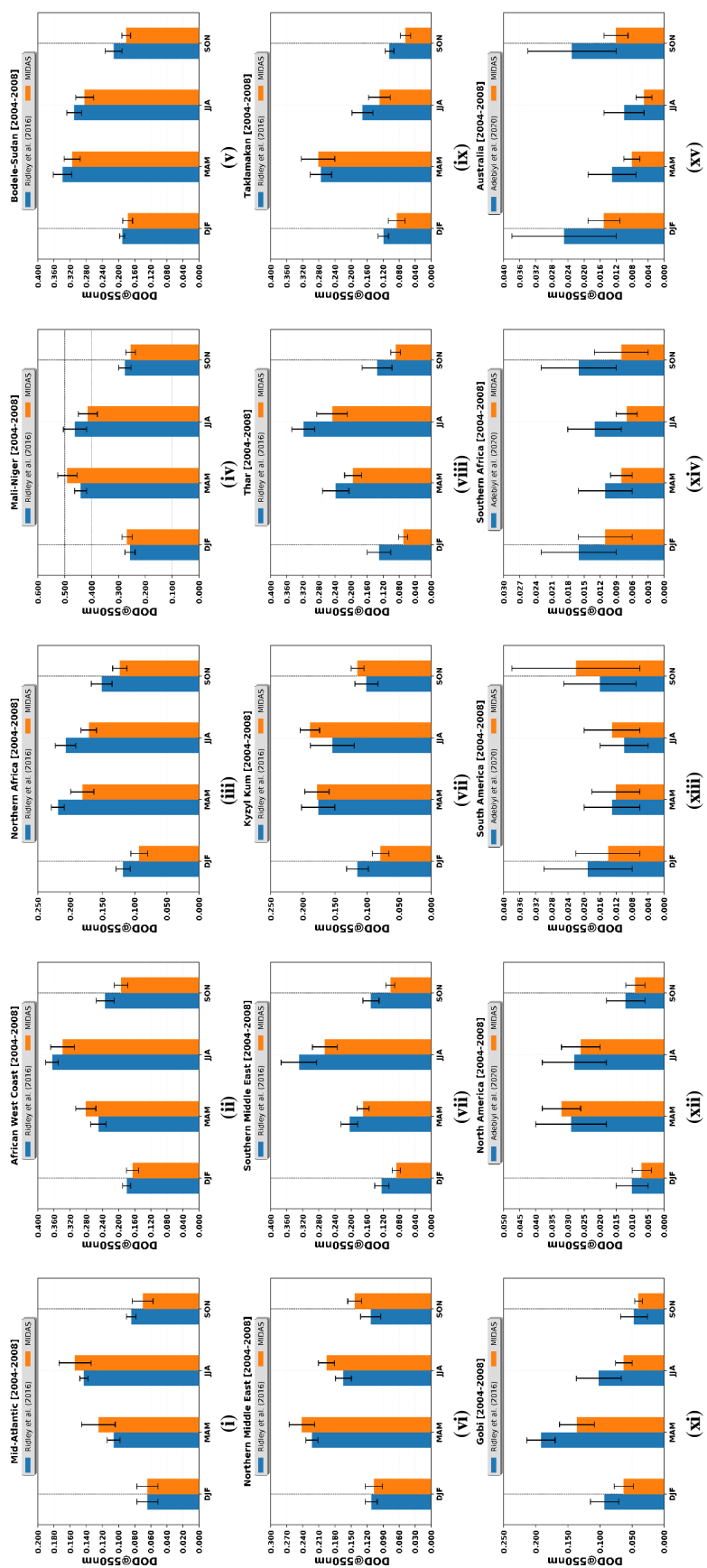


Figure 12: Seasonal DODs, representative for the period 2004 – 2008, based on the MIDAS dataset (orange bars), Ridley et al. (2016) (blue bars) and Adebiji et al. (2020) (blue bars) for 15 regions (their names are given at the top of each plot) defined in Kok et al. (2021a) (see Table 2). The error bars represent the estimated uncertainties. From i to xi, the blue bars correspond to the Ridley et al. (2016) results whereas for the remaining regions MIDAS DODs are compared against the corresponding levels obtained by Adebiji et al. (2020).